Snowfall in the Northern Great Lakes

Lessons Learned from a Multisensor Observatory

Mark S. Kulie, Claire Pettersen, Aronne J. Merrelli, Timothy J. Wagner, Norman B. Wood, Michael Dutter, David Beachler, Todd Kluber, Robin Turner, Marian Mateling, John Lenters, Peter Blanken, Maximilian Maahn, Christopher Spence, Stefan Kneifel, Paul A. Kucera, Ali Tokay, Larry F. Bliven, David B. Wolff, and Walter A. Petersen

ABSTRACT: A multisensor snowfall observational suite has been deployed at the Marquette, Michigan, National Weather Service Weather Forecast Office (KMQT) since 2014. Micro Rain Radar (MRR; profiling radar), Precipitation Imaging Package (PIP; snow particle imager), and ancillary ground-based meteorological observations illustrate the unique capabilities of these combined instruments to document radar and concomitant microphysical properties associated with northern Great Lakes snowfall regimes. Lake-effect, lake-orographic, and transition event case studies are presented that illustrate the variety of snowfall events that occur at KMQT. Case studies and multiyear analyses reveal the ubiquity of snowfall produced by shallow events. These shallow snowfall features and their distinctive microphysical fingerprints are often difficult to discern with conventional remote sensing instruments, thus highlighting the scientific and potential operational value of MRR and PIP observations. The importance of near-surface lake-orographic snowfall enhancement processes in extreme snowfall events and regime-dependent snow particle microphysical variability controlled by regime and environmental factors are also highlighted.

KEYWORDS: Lake effects; Orographic effects; Snowfall; Cloud microphysics; In situ atmospheric observations; Radars/Radar observations

AFFILIATIONS: Kulie—NOAA/NESDIS/STAR/Advanced Satellite Products Branch, Madison, Wisconsin; **Pettersen, Merrelli, Wagner, and Wood**—Space Science and Engineering Center, University of Wisconsin–Madison, Madison, Wisconsin; **Dutter**—NOAA/National Weather Service, Wakefield, Virginia; **Beachler**—NOAA/National Weather Service, Indianapolis, Indiana; **Kluber**—NOAA/National Weather Service, Chicago, Illinois; **Turner**—NOAA/National Weather Service, Marquette, Michigan; **Mateling**—University of Wisconsin–Madison, Madison, Wisconsin; **Lenters**—Michigan Technological University, Houghton, Michigan; **Blanken**—Department of Geography, University of Colorado Boulder, Boulder, Colorado; **Maahn**—Leipzig University, Leipzig, Germany; **Spence**—Environment and Climate Change Canada, Saskatoon, Saskatchewan, Canada; **Kneifel**—University of Cologne, Cologne, Germany; **Kucera**—National Center for Atmospheric Research, Boulder, Colorado; **Tokay**—NASA Goddard Space Flight Center, Greenbelt, Maryland; **Bliven and Wolff**—NASA Wallops Flight Facility, Wallops Island, Virginia; **Petersen**—NASA Marshall Space Flight Center, Huntsville, Alabama

The Laurentian Great Lakes collectively form a vast natural reservoir that strongly influences regional weather and climate in winter months (e.g., Petterssen and Calabrese 1959; Changnon and Jones 1972; Sousounis and Fritsch 1994; Angel and Isard 1998; Notaro et al. 2013). Air–lake interactions enhance snowfall generated by synoptic-scale midlatitude cyclones (i.e., lake-enhanced snow) (Owens et al. 2017) and produce lake-effect snow (LES) from shallow cumuliform clouds during cold air outbreaks (e.g., Holroyd 1971; Niziol et al. 1995; Kristovich and Laird 1998; Kristovich et al. 2003, 2017). Lake-influenced snowfall is an integral component of the Great Lakes hydrologic budget (Scott and Huff 1996; Pettersen et al. 2020a), impacts regional ecology (Henne et al. 2007; Kolka et al. 2010), and socioeconomically affects the ~34 million residents living in the Great Lakes basin (e.g., Schmidlin 1993; Schmidlin and Kosarik 1999). Since Great Lakes snowfall is sensitive to lake ice cover and air–lake temperature differences, long-term temperature trends may modulate winter precipitation in this region (Burnett et al. 2003; Kunkel et al. 2009; Notaro et al. 2014).

Lake Superior is the northernmost and largest Great Lake. It is usually exposed to cold air outbreaks first and preconditions the boundary layer for southern tier Great Lakes—an important process for lake-to-lake LES events that can span hundreds of kilometers (Ballentine et al. 1998; Rodriguez et al. 2007; Laird et al. 2017; Villani et al. 2017; Lang et al. 2018; Kristovich et al. 2018). Lake Superior LES morphology is also somewhat unique, as widespread wind-parallel LES structures occur much more frequently than other Great Lakes (Kristovich and Steve 1995). Lake Superior LES observations, however, serve as plausible proxies for broad coverage LES events over northern Lakes Michigan and Huron that share similar meteorological conditions and shoreline topography.

Michigan's Upper Peninsula—located on Lake Superior's southern shore—receives between ~150 and 750 cm of snow accumulation annually (Fig. 1). Snowfall production is modulated by Lake Superior's proximity, as near-shoreline locales in the Marquette, Michigan, National Weather Service (NWS) Weather Forecast Office (WFO) (hereafter referred to by its radar call sign KMQT) county warning area annually receive 2–4 times more accumulation than southern inland sites.[1] Snow accumulations are orographically amplified by 100–300-m lake surface-to-inland elevation gains (Fig. 1). For example, KMQT—located ~12 km inland and ~200 m higher than Lake Superior—measures over 500 cm of snow accumulation annually, while the lakeshore city of Marquette receives ~300 cm. NWS cooperative observer and snow spotter networks in higher terrain locations measure ~20%–40% more annual snowfall than KMQT.[2]

[1] Site-specific snowfall accumulations are obtained from KMQT data archives: www.weather .gov/mqt/Local_Climate_Information.

[2] Seasonal KMQT snowfall accumulation analyses can be found at the following link: www.weather .gov/mqt/seasonsnowfallmaps.

Motivated by this region's snowfall production and exposure to different snowfall regimes (e.g., synoptic, LES, lake orographic, lake enhanced—see later sections for regime descriptions), in situ microphysics and remote sensing instruments were deployed at KMQT in January 2014 with a snowfall-centric mission (Pettersen et al. 2020a). This observational suite has since operated continuously and complements KMQT and Great Lakes Evaporation Network (GLEN) measurements, thus creating an integrated dataset comprised of snow microphysical properties, radar observations, and meteorological measurements. This manuscript conveys the project's scientific objectives, early scientific lessons learned, and future research plans that will leverage this unique dataset.
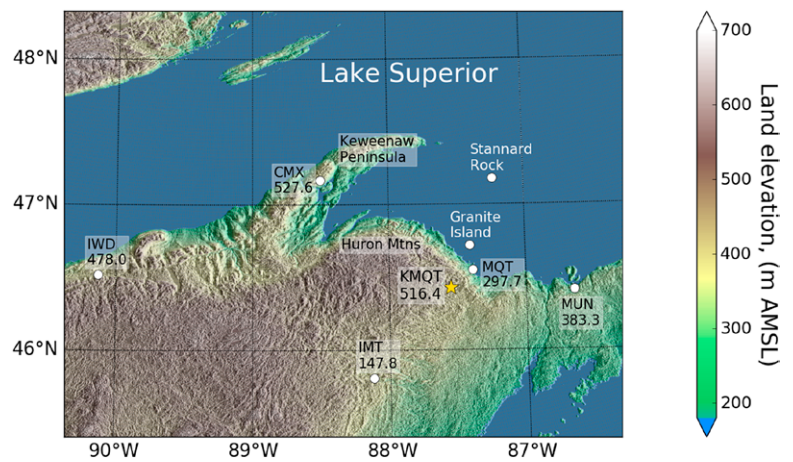

Fig. 1. Land elevation (m) above mean sea level near Michigan's Upper Peninsula. Annual mean snow accumulations (cm) from a 30-yr climatology (1981–2010) are also shown for multiple sites [Ironwood (IWD), Houghton (CMX), Marquette National Weather Service (KMQT), Marquette (MQT), Munising (MUN), and Iron Mountain (IMT)] in the KMQT county warning area. The Granite Island and Stannard Rock Great Lakes Evaporation Network sites are also indicated.

Scientific objectives

Quantifying regime-dependent snow microphysical variability. Snow particle microphysical properties (e.g., particle number concentration, mass, density, fall speed, and microstructure) vary both as a function of size and in bulk due to snowfall regime and associated environmental conditions (e.g., temperature, water vapor content, boundary layer instability, wind speed and direction). The microphysical composition of Lake Michigan and Ontario LES events have been studied with aircraft and ground-based instrumentation (Agee and Hart 1990; Braham 1990; Braham and Dungey 1995; Kristovich et al. 2000; Hudak et al. 2006; Barthold and Kristovich 2011; Wood et al. 2015; Welsh et al. 2016). These studies augment frozen hydrometeor microphysical observations collected worldwide (e.g., Heymsfield et al. 2010; Field et al. 2007; Brandes et al. 2007; Houze et al. 2017; McFarquhar et al. 2017; Schirle et al. 2019). The current study, however, provides a long-term ground-based microphysical perspective of snowfall regimes in a previously uninvestigated northern Great Lakes location.

Quantifying regime-dependent snow accumulation partitioning. The second project goal is quantifying regime-dependent annual snow accumulation percentages. A 50-plus-yr lineage of snowfall regime partitioning studies that use ground-based measurements have quantified the contribution of LES to annual snowfall amounts and long-term LES trends throughout the Great Lakes region. Seasonal analyses estimate about 30%–60% of the annual snowfall accumulation on Lake Michigan's leeward shoreline can be attributed to LES (Eichenlaub 1970; Braham and Dungey 1984). Veals and Steenburgh (2015) calculated LES annual snowfall contributions of 61%–76% in Lake Ontario snowbelts using daily snowfall measurements and operational radar datasets. Pettersen et al. (2020a) reported shallow snow event frequency and annual accumulation percentages of 68% and 49%, respectively, using 1-min KMQT observations. Great Lakes LES activity has also increased throughout much of the twentieth century (Eichenlaub 1970; Braham and Dungey 1984; Norton and Bolsenga 1993; Leathers and Ellis 1996), although lake-influenced snowfall trends and synoptic weather patterns that are conducive to LES production have

decreased after the early 1980s (Bard and Kristovich 2012; Suriano and Leathers 2017a,b; Suriano 2019).

The aforementioned surface-based studies in the Great Lakes region, combined with observational studies that quantify regime-dependent annual snowfall accumulation statistics over high-latitude ice sheets (Gorodetskaya et al. 2013; Pettersen et al. 2018), illustrate the hydrologic impacts of different snowfall regimes. These studies also serve as valuable datasets to assess regime-dependent snow event detection and quantitative precipitation estimates (QPE) from spaceborne instruments (Maahn et al. 2014). Satellite observations indicate that shallow cumuliform snowfall (e.g., LES and ocean-effect snow) comprises greater than 50% of estimated snow event occurrence and annual accumulation in many higher latitude regions (Kulie et al. 2016; Kulie and Milani 2018; West et al. 2019). Satellite-derived datasets can be further vetted using specialized datasets collected at sites like KMQT.

Improving snowfall QPE. Snow microphysical composition controls the bulk microwave scattering properties associated with surface snowfall events (e.g., Liu 2008a; Kulie et al. 2010; Kneifel et al. 2011a; Leinonen et al. 2012; Kulie et al. 2014; Kneifel et al. 2015; Olson et al. 2016; Matrosov et al. 2019). Ground-based radar QPE is essential for hydrologic monitoring, yet operational radar network products like the Multi-Radar Multi-Sensor (MRMS; Zhang et al. 2016) currently adopt a static reflectivity Z ($mm^6 m^{-3}$) to liquid-equivalent snowfall rate[3] S (mm h^{-1}) conversion for snowfall. Other Z–S conversions are applied at the discretion of local NWS WFOs (Ryzhkov and Zrnić 2019). The wide range of Z–S conversions reflect underlying microphysical variability and resulting uncertainty (Matrosov 2007; Liu 2008b; Kulie and Bennartz 2009; Matrosov et al. 2009; Hiley et al. 2011; Wolfe and Snider 2012; Huang et al. 2015; von Lerber et al. 2017; Cooper et al. 2017). A primary objective of the KMQT dataset is refining regime-dependent Z–S conversions to improve radar QPE.

Satellite-based snowfall QPE has also received ample attention in recent years due to the *CloudSat* (Stephens et al. 2008, 2018) and Global Precipitation Measurement (GPM; Hou et al. 2014; Skofronick-Jackson et al. 2017) missions. Satellite precipitation retrievals rely on microphysical assumptions that translate radar and passive microwave measurements to surface snowfall rates (Kummerow et al. 2015; Wood et al. 2015; Grecu et al. 2016; Liao et al. 2016; Meng et al. 2017; Skofronick-Jackson et al. 2019; Ringerud et al. 2019; Wood and L'Ecuyer 2020). Snow microphysics and coincident remote sensing observations are therefore important informational conduits for improving spaceborne QPE algorithms.

[3] Unless explicitly noted otherwise, snowfall rates are assumed to be liquid-equivalent rates throughout the manuscript. Liquid-equivalent snowfall rates are also referred to as snow water equivalent (SWE) precipitation rates in the literature. SWE is not used in this study to avoid confusion with the hydrologic SWE definition for the total melted water contained in accumulated ground snowpack.

Observations
Profiling radar. The Micro Rain Radar 2 (MRR) is a K-band (24 GHz) profiling radar (Klugmann et al. 1996). MRRs have been successfully used in many snowfall studies (Keighton et al. 2009; Kneifel et al. 2011b; Gorodetskaya et al. 2013; Stark et al. 2013; Colle et al. 2014; Maahn et al. 2014; Minder et al. 2015; Skofronick-Jackson et al. 2015; Souverijns et al. 2017; Schirle et al. 2019; Pettersen et al. 2020a). The MRR provides radar reflectivity, Doppler velocity V_D spectra, and Doppler spectrum width σ_D profiles in 31 range gates at 1-min intervals. Postprocessing steps optimize MRR reflectivities for snowfall with a minimum detectable signal of about −10 dBZ (Kneifel et al. 2011a; Maahn and Kollias 2012). Further MRR specifications are provided in previous studies (Kneifel et al. 2011a; Maahn and Kollias 2012; Pettersen et al. 2020a).

The KMQT MRR uses 100-m range gates and samples up to 3 km above ground level (AGL). MRR profiles augment the scanning KMQT Next Generation Weather Radar (NEXRAD) Weather

Surveillance Doppler Radar observations, especially since the KMQT NEXRAD has historically operated in a "clear air" (five elevation angles) scanning mode with limited vertical information near the radar for most snowfall events (Pettersen et al. 2020a). The measurements in the fourth range gate (300–400 m AGL) are defined as "near-surface" MRR observations to avoid ground clutter.

Precipitation particle imager. The Precipitation Imaging Package (PIP)—an updated version of the Snowflake Video Imager (SVI; Newman et al. 2009)—is an imaging disdrometer that provides two-dimensional imagery of hydrometeor shadows using a high-speed camera (Pettersen et al. 2020b). The PIP is relatively immune to wind-related collection issues due to its open instrument design—a distinct advantage compared to other devices (Battaglia et al. 2010). Automated tracking software measures individual particle dimensions and particle fall speeds. The PIP provides 1-min averaged particle size distributions (PSD) for particle diameters D_{eq}, as well as mean liquid equivalent snowfall rate and effective bulk particle density estimates (Pettersen et al. 2020b). The D_{eq} is defined as the diameter of a circle with an area equal to that of the projected particle (Wood et al. 2013; von Lerber et al. 2017; Pettersen et al. 2020b). Additional PIP details are provided in previous studies (Kneifel et al. 2015; Tiira et al. 2016; Souverijns et al. 2017; von Lerber et al. 2017, 2018; Pettersen et al. 2020a,b). Figure 2 shows the MRR and PIP deployment configuration at KMQT. KMQT PIP and MRR data can be obtained from the NASA Global Hydrology Research Center archive (https://ghrc .nsstc.nasa.gov/home/). Daily quick-look images are available at the following site: www .ssec.wisc.edu/lake_effect/mqt/.

KMQT observations. The KMQT site was chosen primarily for its perennially consistent snowfall. More practically, KMQT also provides reliable power, internet connectivity, meteorological expertise, and valuable observations. A scanning S-band, dual-polarization NEXRAD is located at KMQT. Standard meteorological observations are also collected. NWS staff measure snow accumulation every six hours using a snow board. Liquid water equivalent (LWE) measurements are obtained from melted snow collected in a standard 20-cm precipitation gauge with a wind shield. An OTT Pluvio 200 precipitation weighing gauge is also deployed at KMQT. This gauge is part of a larger Pluvio network deployed near KMQT during the 2017–20 winters. An Automated Weather Observing System (AWOS) is also located at a nearby airport (~25 km).

Over-lake meteorological and flux observations. Eddy covariance instrumentation measures over-lake sensible and latent heat fluxes and standard meteorological variables at the Granite Island and Stannard Rock GLEN sites (Blanken et al. 2011; Spence et al. 2011, 2013). Granite Island (Stannard Rock) is located about ~25 (75) km northeast (north-northeast) of KMQT (Fig. 1). Eddy covariance data are collected at a 10-Hz rate and processed to 30-min fluxes. Data can be obtained from the GLEN archive site (https://superiorwatersheds.org /GLEN/data.htm). Lake temperature and ice coverage are obtained from Great Lakes

Fig. 2. KMQT instrument deployment configuration.

Environmental Research Laboratory daily analyses (https://coastwatch.glerl.noaa.gov/). Nearby operational radiosondes (e.g., Gaylord, Michigan; International Falls, Minnesota) provide atmospheric temperature profile measurements.

Shallow snow, deep implications

The KMQT observatory reveals a critical aspect of northern Great Lakes snowfall: snowfall produced from clouds with shallow precipitation echo-top heights (PETH) is ubiquitous and hydrologically important. Pettersen et al. (2020a) highlights a distinct shallow snowfall mode that comprises almost 70% of all KMQT snowfall events. Pettersen et al. (2020a) also show that near-surface MRR reflectivity Z_{sfc} values associated with KMQT shallow snow events are ~10 dB smaller than deep events, yet shallow events account for ~50% of the mean annual KMQT snowfall accumulation.

Postfrontal LES—mostly multiband "broad coverage" events (e.g., Kelly 1982, 1984, 1986; Kristovich 1993; Kristovich and Steve 1995; Veals and Steenburgh 2015)—are the most common KMQT shallow snowfall type. While light snowfall rates accompany most KMQT LES events, LES can produce heavy and blowing snow that warrant hazardous winter weather advisories. Additionally, individual LES events can persist for several days. KMQT instruments observed single LES events that spanned ~76 (3–6 January 2018) and ~90 (17–21 January 2019) hours. Shallow snow—primarily LES—dominated the KMQT meteorological landscape in January 2019 by occurring on 22 of 31 days and comprising ~40% of all MRR observations.

Figures 3 and 4 show a prototypical broad coverage LES event to illustrate the unique capabilities of the KMQT observational suite. This event developed in the wake of a strong surface cyclone that tracked northeastward over the region between 18 and 20 November 2016 (see supplementary Fig. ES1 for surface pressure and wind animations; https://doi.org/10.1175/BAMS-D-19-0128.2). A vigorous cold front passed KMQT near 0100 UTC 19 November, with postfrontal 10-m air temperatures T_{10m} between –4° and –7°C and rapidly rising surface pressures (Fig. 3f). Lake Superior water (5°–10°C) and estimated 850-hPa (–10°C) temperature differences were ~15°–20°C, well above the 13°C threshold for likely LES development (Niziol et al. 1995). North-northwesterly (NNW) surface winds were sustained between 10 and 15 m s^{-1} before 2000 UTC 19 (Fig. 3g), then subsided and shifted directions [north (N)]. Multiple winter weather warnings and advisories for heavy snow and high winds were issued throughout this event. KMQT measured over 23 cm of accumulated snow between 1800 UTC 19 and 1800 UTC 20 November.

KMQT NEXRAD imagery showed LES bands after ~1000 UTC 19 November (Fig. 4; also see supplementary Fig. ES2 for an event radar animation). Both 0.5° and 1.5° elevation angles are shown since terrain-induced 0.5° beam blockage occurs in some sectors. The shallow nature of LES bands is also emphasized by showing both elevation angles, as many 0.5° features are absent in 1.5° observations at distances greater than ~75–100 km from KMQT. An intense snowband was located ~60 km east of KMQT at 2116 UTC 19 November (Figs. 4a,b). Widespread synoptic snow remnants were located further east. Enhanced, nonbanded reflectivity structures were also anchored along the Lake Superior shoreline near KMQT—a probable lake-orographic enhancement signal (Figs. 4a,b). Multiple intense LES bands persisted on 20 November 2016 (Figs. 4c,d).

MRR reflectivity profiles further highlight this event's shallow and transitory features (Fig. 3a). PETH values peaked between ~1.5 and 1.7 km before ~2300 UTC 19 November. MRR Z_{sfc} values exceeded 20 dBZ, but without obvious cellular structures, during the lake-orographic period (~1600–2230 UTC 19 November) that was also illustrated in NEXRAD imagery (Figs. 4a,b). These trends are similar to orographically induced MRR reflectivity structural changes observed in LES near Lake Ontario (Minder et al. 2015; Welsh et al. 2016), although coastal baroclinic processes also likely contribute to these reflectivity features
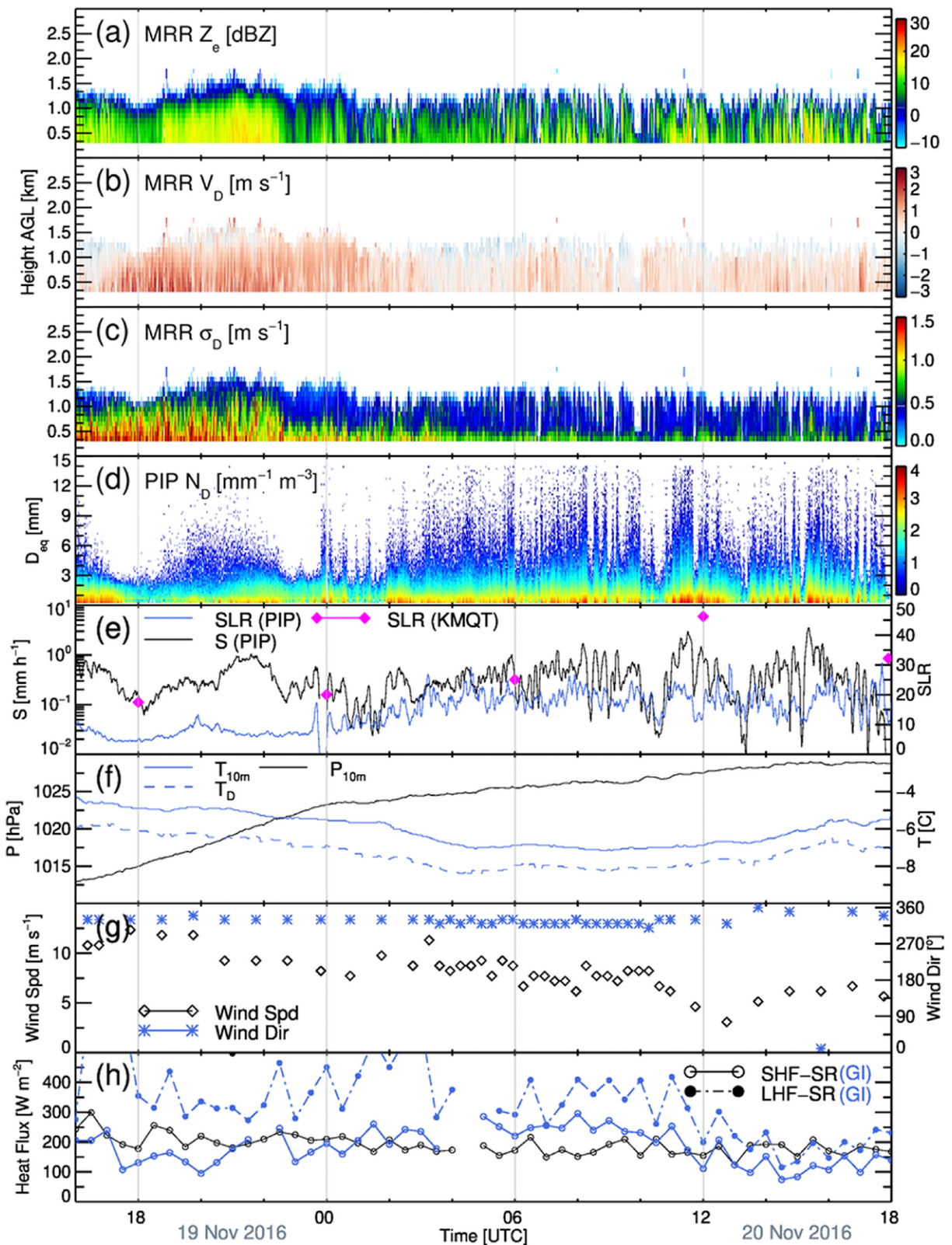
Fig. 3. Micro Rain Radar (a) radar reflectivity (dB*Z*), (b) Doppler velocity (m s⁻¹), and (c) Doppler spectrum width (m s⁻¹) profiles for the 19–20 Nov 2016 LES event. PIP-derived 1-min (d) particle number concentration as a function of particle size (colored in logarithmic units; mm⁻¹ m⁻³), (e) liquid equivalent snowfall rates *S* (mm h⁻¹; black), and snow-to-liquid ratio (SLR; blue) are also shown. KMQT NWS 6-hourly SLR measurements are also indicated (magenta diamonds). The following meteorological observations are also illustrated: (f) KMQT 10-m temperature (°C; blue solid), dewpoint temperature (°C; blue dashed), and atmospheric pressure (hPa; black); (g) AWOS 10-m wind speed (m s⁻¹; black) and direction (blue); (h) sensible (SHF; solid) and latent (LHF; dashed) heat fluxes (W m⁻²) measured at the Granite Island (GI; blue) and Stannard Rock (SR; black) Great Lakes Evaporation Network sites.
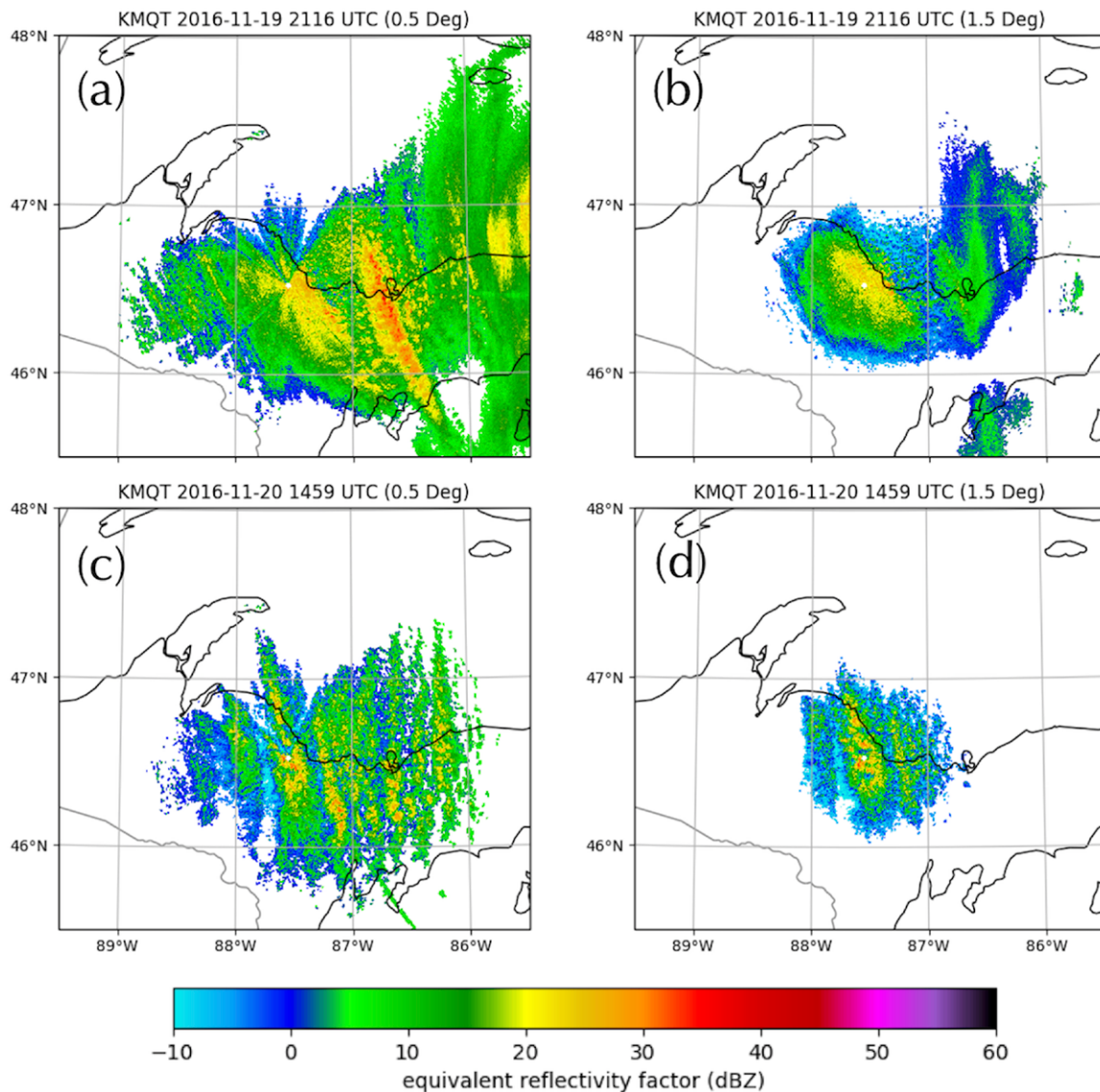
Fig. 4. KMQT NEXRAD (a) 0.5° and (b) 1.5° radar reflectivities for 2116 UTC 19 Nov 2016. (c),(d) The same NEXRAD observations for 1459 UTC 20 Nov 2016. NEXRAD figures are created using the Python ARM Radar Toolkit (Helmus and Collis 2016).

(Campbell and Steenburgh 2017; also see the following section for further discussion). MRR reflectivity structures evolved into distinct, periodic convective cores after ~2230 UTC 19 November. After a period of lower intensity MRR reflectivities and PIP-measured snowfall rates (Fig. 3e), LES bands reinvigorated after ~1000 UTC. The Z_{sfc} values again exceeded 20 dBZ. Near-surface MRR σ_D values exceeded 1.5 m s^{-1} (Fig. 3c) and over-lake sensible (~300–700 W m^{-2}) and latent (~100–300 W m^{-2}) heat fluxes (Fig. 3h) confirmed vigorous air–lake interactions and a turbulent boundary layer under ice free conditions. PETH values near 1.5 km represent the upper end of the KMQT PETH spectrum for LES events (e.g., Fig. 6a), but are shallower than more vigorous LES events that occur in the southern Great Lakes (Minder et al. 2015; Kristovich et al. 2017).

PIP measurements revealed a distinct microphysical transition throughout this event. For instance, particle concentrations increased for $D_{eq} > $ ~6 mm and $D_{eq} < $ ~1 mm particle sizes after 2230 UTC 19 November (Fig. 3d). Maximum particle sizes exceeded 12 mm in LES cores. PIP-derived S surpassed 1 mm h^{-1} on 19 November, while peak S values exceeded 3 mm h^{-1} after 1000 UTC 20 November with notable S variability over short time scales (Fig. 3e). Conversely, the earlier lake-orographic phase displayed much lower temporal S variability.

PIP-estimated snow-to-liquid ratios[4] (SLR; Pettersen et al. 2020b) also steadily increased from ~10 to ~15–25 (Fig. 3e). KMQT SLR trends were similar, but were consistently higher and reflect inherent measurement differences (e.g., settling, snowflake packing, and wind effects may affect 6-h KMQT observations). SLR trends replicated snow particle density changes inferred from lower MRR V_D values observed on 20 November (Fig. 3b). The PIP estimated 9.9 mm LWE accumulation in the 24-h period after 1800 UTC 19 November, while KMQT measured 7.4 mm (Table 1).

A little orography goes a long way

While broad coverage LES constitute most KMQT shallow snow events, another shallow snowfall regime that is caused by combined lake-orographic influences is observed at this site. Even though the ~200-m elevation gain from Lake Superior to KMQT that is somewhat insignificant when compared to mountainous regions, orography increases snowfall production at KMQT and throughout the Great Lakes by mechanically inducing upward air parcel motion, increasing local relative humidity values, instigating or enhancing cloud and precipitation particle growth processes, and reducing subcloud sublimation (Minder et al. 2015; Veals and Steenburgh 2015; Villani et al. 2017; Veals et al. 2018). Figure 5 illustrates daily LWE totals collected by a network of 10 Pluvio precipitation weighing gauges deployed near KMQT during an orographically influenced snowfall event. The two gauges closest to Lake Superior (3 and 7) recorded ~5–7 mm LWE, while gauges sited just west of the largest elevation gradients (4, 10, KMQT) measured LWE exceeding 12 mm. These daily snowfall patterns replicate the mean annual snowfall accumulations shown in Fig. 1.

Orographic processes near KMQT are further enhanced by lake-driven processes. Increased boundary layer moistening results from air–lake interactions, while coastal mesoscale circulations can be induced by land–water thermal contrasts (e.g., Campbell and Steenburgh 2017). Following Veals and Steenburgh (2015), the "lake-orographic" moniker is applied to shallow snowfall events at KMQT that fall within the lake-effect precipitation spectrum, but are distinguished from broad

[4] SLR refers to the ratio between accumulated snow and its melted liquid water equivalent and is inversely related to bulk snow density.

Table 1. KMQT LWE (mm) measurements and PIP LWE (mm) estimates for four snowfall events highlighted in this study.

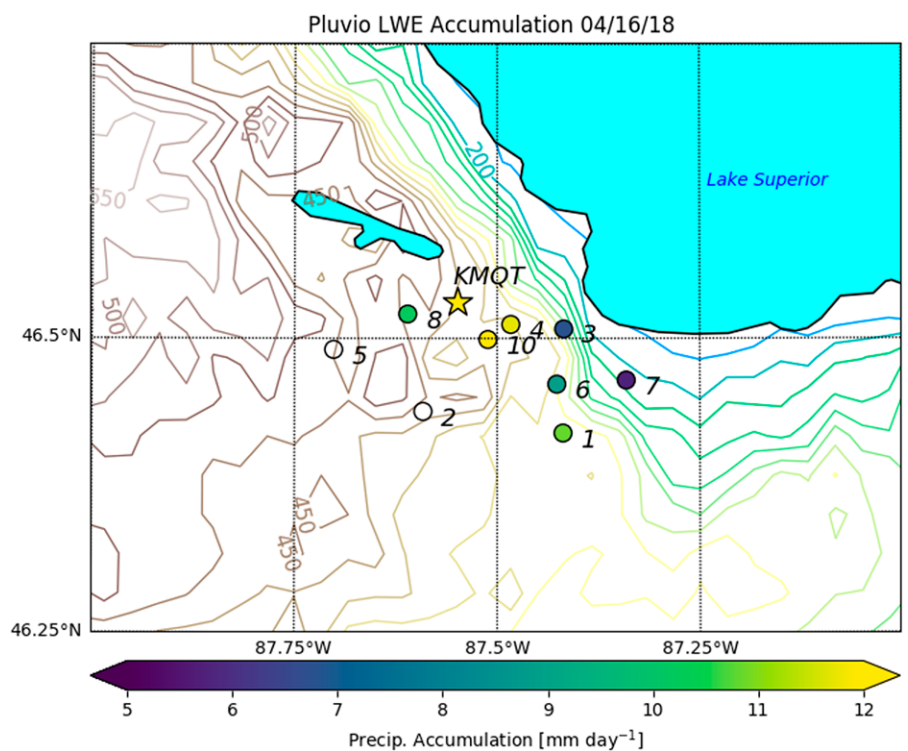| KMQT snowfall events	KMQT	PIP
Lake effect: 1800 UTC 19–1800 UTC 20 Nov 2016	7.4	10.0
Lake orographic: 0000–1200 UTC 8 Mar 2014	2.3	1.9
Transition: 1200 UTC 13–0600 UTC 14 Dec 2017	5.8	7.2
Lake enhanced: 1800 UTC 10–1800 UTC 12 Nov 2014	82.3	94.3

Fig. 5. The 16 Apr 2018 daily liquid water equivalent (LWE) accumulations from a Pluvio weighing gauge network deployed near KMQT. Sites 2 and 5 did not report any accumulations due to instrument power-related issues.

coverage LES by the following four characteristics: 1) spatially contiguous NEXRAD reflectivity features confined mostly to land, 2) embedded NEXRAD reflectivity maxima within the broader contiguous reflectivity field aligned with the nearshore topographical gradient, 3) shallow MRR reflectivity structures lacking distinct periodicity, and 4) surface winds typically emanating from the northeast (NE) quadrant. KMQT lake-orographic snow events are less common than broad coverage LES since NE winds occur less frequently than other shallow event wind directions (Pettersen et al. 2020a).

Using the aforementioned distinguishing characteristics to classify snowfall events, composite KMQT MRR reflectivity-height statistics from 194 broad coverage LES and 32 lake-orographic events between January 2014 and April 2018 were created (Figs. 6a,b). The large population of MRR reflectivity observations below ~1 km AGL confirms both lake-orographic and broad coverage LES as KMQT shallow snowfall types shown in Pettersen et al. (2020a). However, lake-orographic Z_{sfc} values are generally ~4–6 dB larger than LES. Mean reflectivity profiles increase substantially toward the ground in the lowest ~1 km AGL for both lake-orographic (>10 dB km^{-1}) and LES (~7–10 dB km^{-1}) events, implying rapid near-surface microphysical changes. Steep near-surface reflectivity gradients also portend spaceborne radar detection difficulties and/or possible QPE biases due to observational blind zones created by ground clutter contaminated range gates directly above the surface
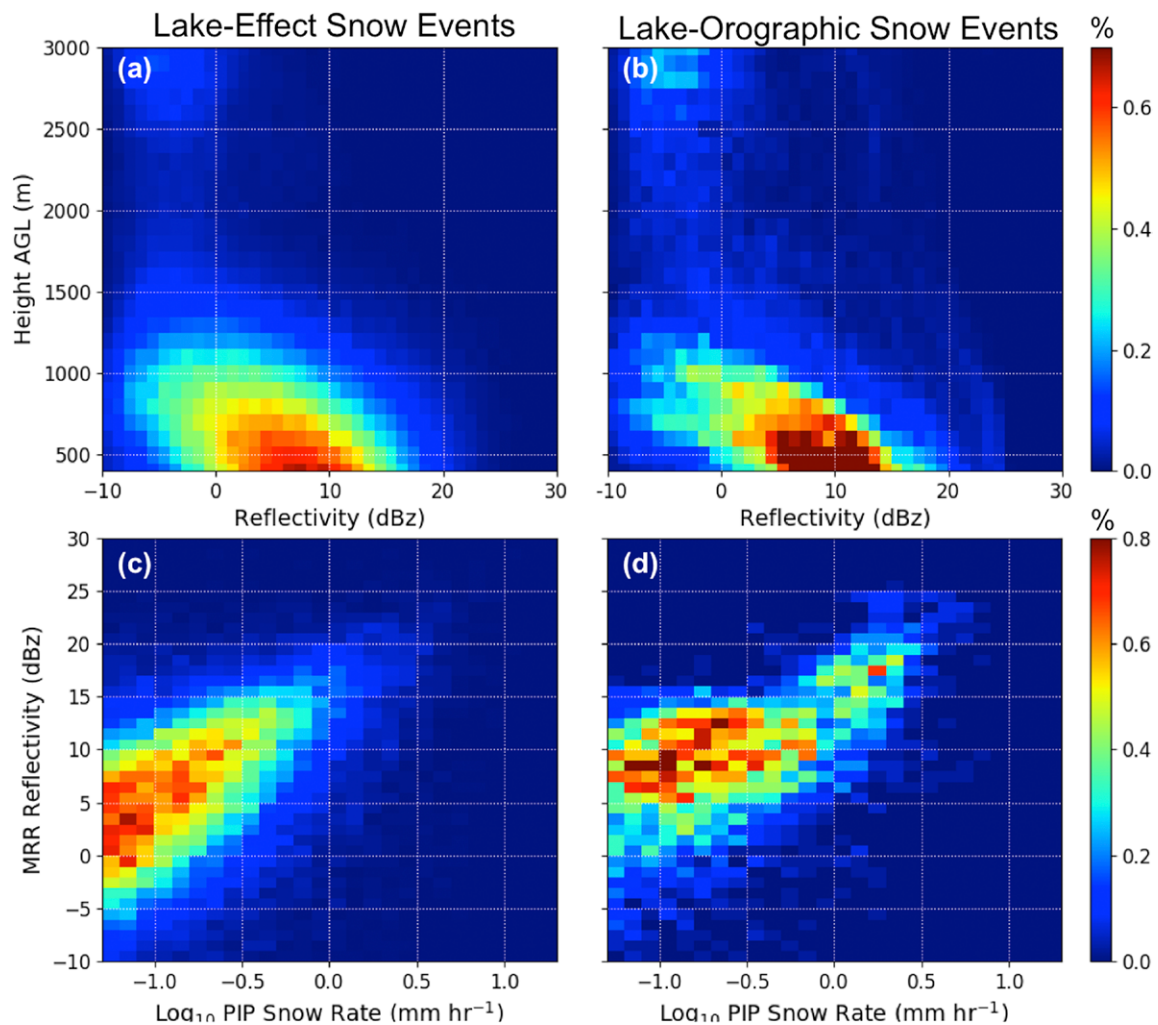

Fig. 6. MRR radar reflectivity–height two-dimensional relative frequency (%) histograms for KMQT (a) LES and (b) lake-orographic snowfall events during the January 2014 through April 2018 period. MRR near-surface reflectivity Z_{sfc}–PIP liquid equivalent snowfall rate S relative frequency histograms are also shown for (c) LES and (d) lake-orographic snowfall events.

(Kulie and Bennartz 2009; Maahn et al. 2014). For instance, GPM Dual-Frequency Precipitation Radar (DPR) radar blind zones range from ~500 m (nadir scan) to over 2 km (off-nadir scans). The near-nadir scanning *CloudSat* Cloud Profiling Radar has ~700 m (ocean) to ~1 km (land) blind zones. QPE derived from the first usable spaceborne range gate might not detect KMQT shallow snow events if PETH values are too low, or might produce biased QPE that does not account for large near-surface reflectivity increases. Additionally, most KMQT shallow snow cannot be detected by the GPM DPR that has a nominal radar sensitivity of ~12 dBZ (Hamada and Takayabu 2016). Radar-based QPE is prone to further regime-dependent uncertainties. Varying MRR Z_{sfc} and PIP-derived S relationships for LES (Fig. 6c) and lake-orographic snow (Fig. 6d) further complicates radar-based QPE without prior knowledge of snowfall regime. Lake-orographic Z–S relationships are highly variable and produce higher snowfall rates than LES events. Furthermore, lake-orographic Z_{sfc} values consistently exceed LES, yet produce similarly light snowfall rates below ~0.3 mm h^{-1} (−0.5 on the log$_{10}$ scale shown in Fig. 6).

The KMQT observational suite has also documented extremely high SLR values during some lake-orographic snowfall events. Figures 7 and 8 highlight a lake-orographic snowfall event that occurred on 8 March 2014 under very cold postfrontal conditions (supplementary Fig. ES3). Lake Superior was almost completely ice covered during an extremely cold winter, with some open waters located near the southern shore (Fig. ES4). Over-lake fluxes were therefore limited (Fig. 7d), but boundary layer moistening and possible coastal baroclinic processes initiated by open water located south of Granite Island produced persistent snowfall for over 10 h (Fig. 7c). Light NEXRAD reflectivities were observed over land with enhanced
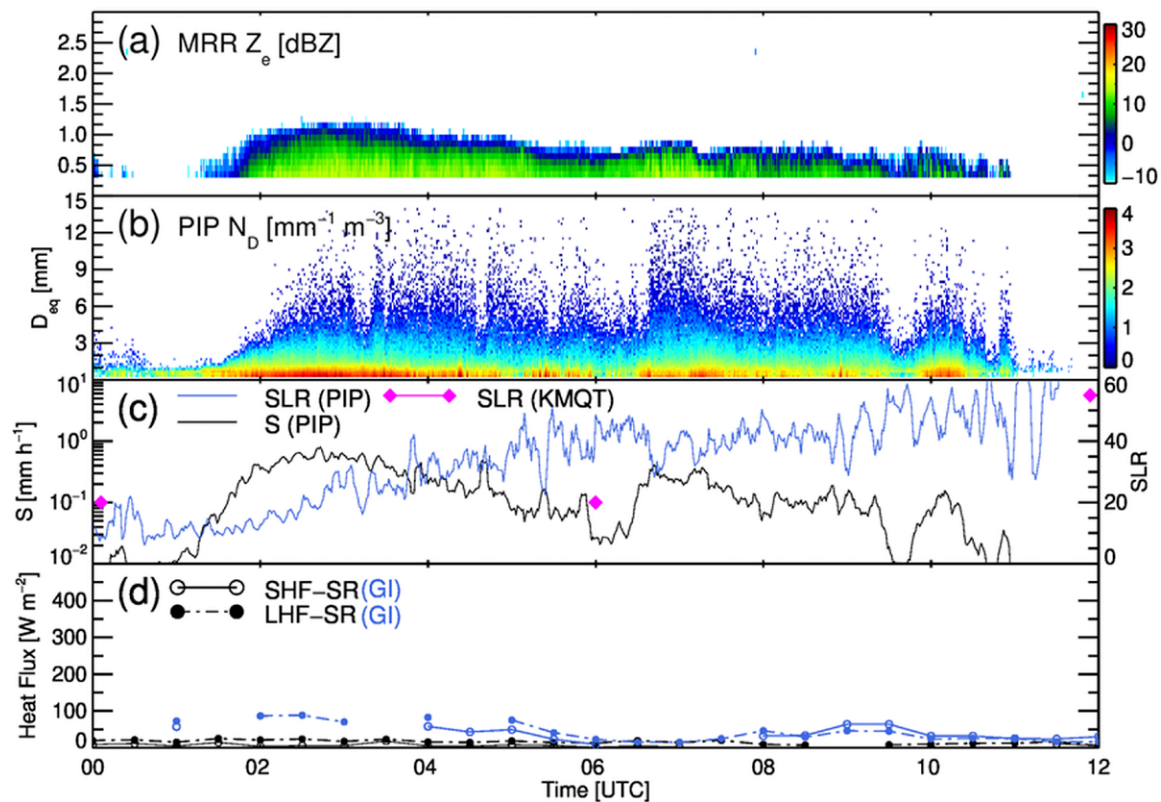

Fig. 7. (a) Micro Rain Radar radar reflectivity (dBZ) profiles, (b) PIP particle number concentration as a function of particle size (colored in logarithmic units; mm^{-1} m^{-3}), (c) PIP liquid equivalent snowfall rates S (mm h^{-1}; black), PIP snow-to-liquid ratio (SLR; blue), and KMQT NWS 6-hourly SLR measurements (magenta diamonds), and (d) sensible (SHF; solid) and latent (LHF; dashed) heat fluxes (W m^{-2}) measured at the Granite Island (GI; blue) and Stannard Rock (SR; black) Great Lakes Evaporation Network sites for the 8 Mar 2014 lake-orographic snowfall event.

values (~15–20 dBZ) anchored near KMQT (Fig. 8, Fig. ES5). MRR PETH values varied between ~0.6 and 1.2 km AGL, but MRR reflectivities lacked distinct periodicity for most of the event (Fig. 7a). The PIP, however, measured very large particles (D_{eq} > 10 mm) (Fig. 7b). A persistent supply of smaller particles also existed, but notable disruptions occurred (e.g., near 0530 UTC). PIP-derived SLRs increased from ~10 to over 40 (Fig. 7c) as temperatures decreased from −5° to −12°C throughout the event (not shown). KMQT measured similar SLR trends (Fig. 7e), including a 55 SLR value under difficult measurement conditions (windy conditions and low density snow). The steady PIP SLR increase from 0000 to 0600 UTC is masked within the KMQT measurement window and highlights the benefit of higher temporal PIP SLR observations to monitor real-time trends.
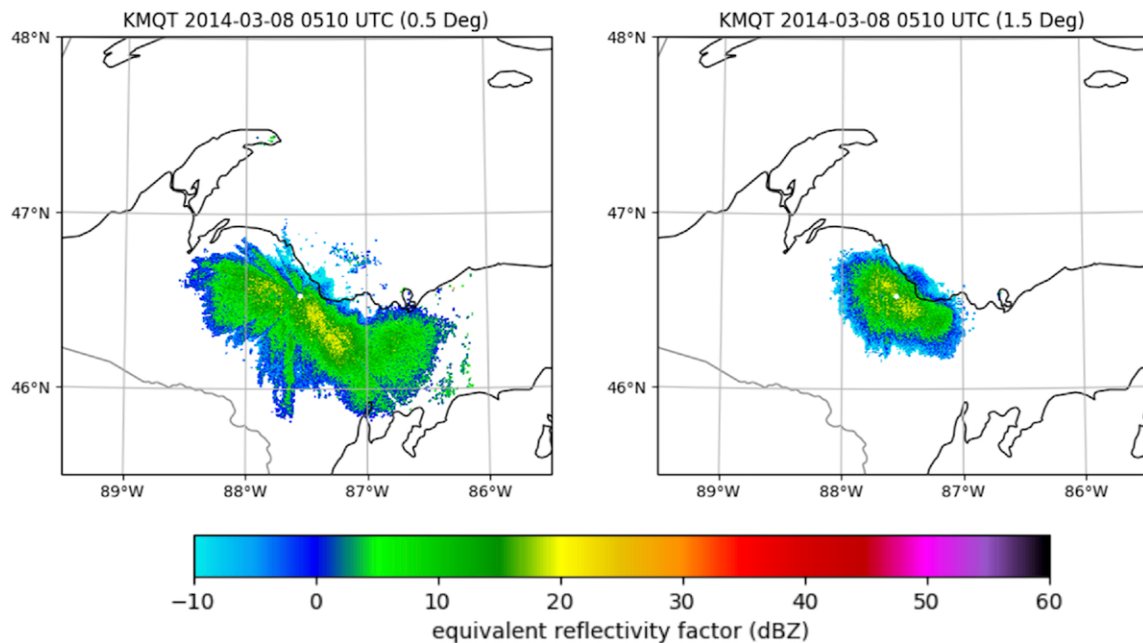
Fig. 8. KMQT NEXRAD 0.5° and 1.5° radar reflectivities at 0510 UTC 8 Mar 2014.

Flipping the microphysical switch

Nature often flips a metaphorical switch when abrupt microphysical transitions accompany snowfall regime transitions. Figure 9 documents a KMQT snowfall event that exhibits snow microphysical variability induced by regime-dependent processes. An "Alberta clipper" (Thomas and Martin 2007) system tracked southeastward from Canada through the southern Great Lakes on 13–14 December 2017 (Fig. ES6). This system initially produced a spatially extensive area of synoptically forced snow (Fig. ES7) and MRR-indicated fall streaks before 1800 UTC 13 December (Fig. 9a).

Combined MRR and PIP observations revealed a dramatic transition between 1800 and 2000 UTC. MRR reflectivities aloft rapidly weakened as the Alberta clipper exited, but near-surface reflectivity enhancements appeared after 1800 UTC (Fig. 9a). MRR reflectivities increased ~6 dB km^{-1} in the lowest 2 km AGL from 1800 to 2000 UTC, compared with ~0.7 dB km^{-1} from 1000 to 1800 UTC. MRR σ_D values also increased (Fig. 9c), likely indicating boundary layer turbulence invigorated by increased fetch across Lake Superior under east-northeast (ENE) winds (Fig. 9f). Natural seeder–feeder particle growth processes (i.e., light snow particles generated aloft seeding shallow boundary layer clouds; Schroeder et al. 2006) plausibly combined with lake-orographic enhancement processes to intensify snowfall rates. NEXRAD imagery near 1830 UTC also showed a reflectivity enhancement zone anchored near KMQT (Fig. ES7).
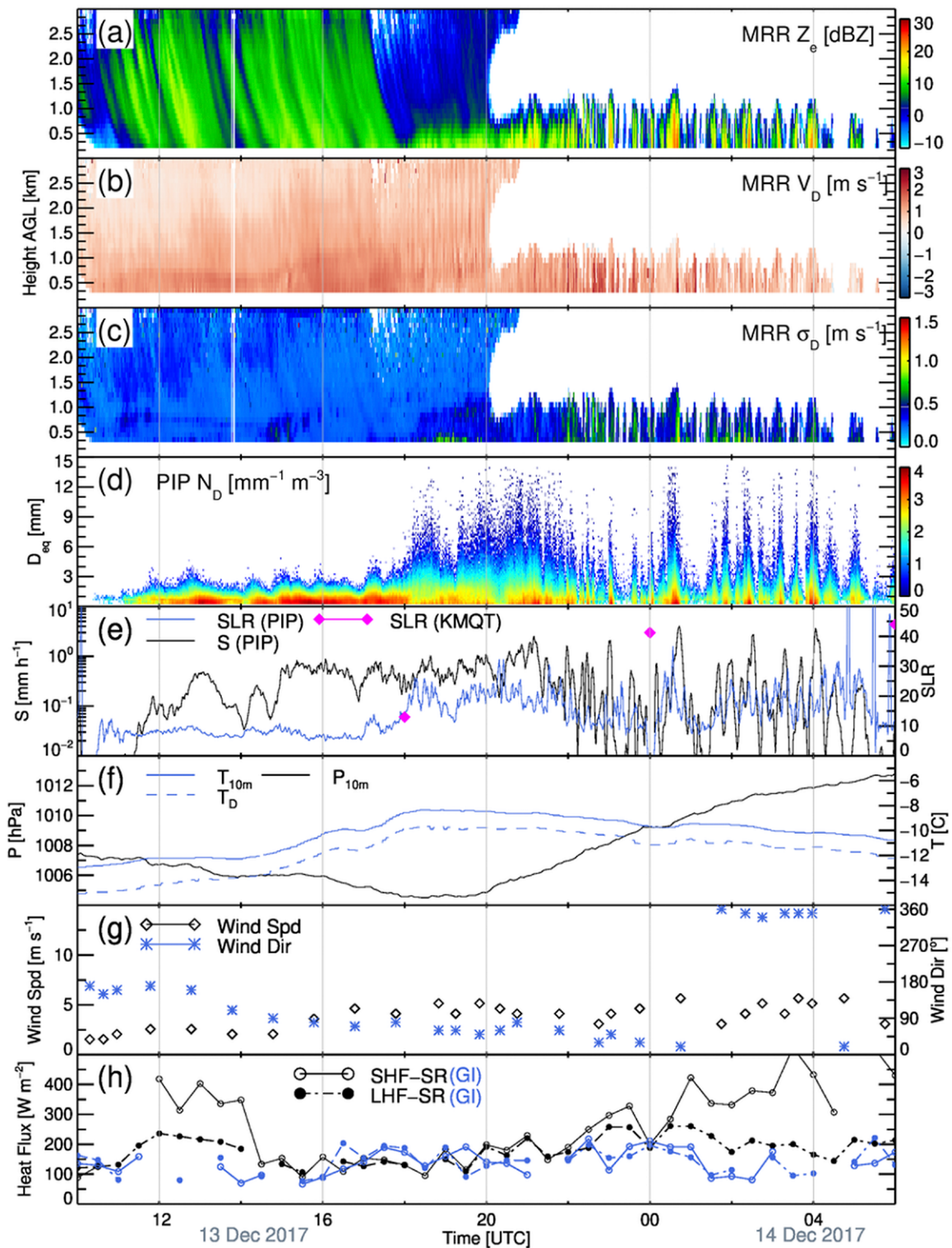
Fig. 9. As in Fig. 3, but for the 13–14 Dec 2017 transition event.

The PIP revealed abrupt microphysical changes near 1800 UTC. Maximum D_{eq} values immediately increased from ~3–5 mm to ~10–15 mm. Particle concentrations in the ~3–6 mm D_{eq} range also increased, while the $D_{eq} < $ ~1 mm particle population decreased by almost an order of magnitude (Fig. 9d). PIP-derived SLR also increased and oscillated between ~15 and 25 between 1800 and 2000 UTC. Increasing SLR values conformed with near-surface MRR V_D reductions from 1600–1800 UTC to 1800–2000 UTC (Fig. 9b). Despite starkly different microphysical composition, PIP S (~0.5–1.0 mm h^{-1}) and MRR Z_{sfc} (~10–15 dBZ) values did not change appreciably. Temperatures increased by ~2°C between 1600 and 1800 UTC as

winds shifted from ESE to ENE, allowing air parcel trajectories over unfrozen Lake Superior (Figs. 9f,g). Over-lake fluxes oscillated between ~100 and 225 W m^{-2} between 1600 and 2000 UTC (Fig. 9h), confirming active surface energy exchanges. Lake-induced snowfall enhancements, however, did not occur until the wind direction shifted to ENE after 1800 UTC (Fig. 9g).

A final transition to banded, shallow LES occurred after ~2000 UTC as wind direction shifted from ENE to N and over-lake fluxes increased (300–400 Wm^{-2}; Figs. 9a,g,h). PIP PSDs broadened further (Fig. 9d), and PIP-measured S exceeded 2 mm h^{-1} (Fig. 9e). PIP SLR values varied between ~10 and 30 and were anticorrelated with S in most LES cores, indicating possible rimed particles (Fig. 9e). KMQT SLR measurements matched PIP trends, although KMQT values were at least double during the LES stage. KMQT measured 17.2 cm of accumulated snow (5.8-mm LWE) between 1200 UTC 13 and 0600 UTC 14 December, while the PIP estimated 7.1-mm LWE (Table 1).

Regime-dependent microphysical variability can be explored further using the multiyear KMQT dataset. Following the Pettersen et al. (2020a) partitioning methodology, deep (MRR PETH ≥ 3 km) and shallow (PETH < 3 km) snow event SLR statistics are shown in Fig. 10 as a function of PIP-derived PSD parameters. The following inverse exponential function is often used to describe snow PSDs: $N(D) = N_o \exp(-\Lambda D)$, where N is the particle concentration (mm^{-1} m^{-3}) for a given particle diameter D, and N_o (mm^{-1} m^{-3}) and Λ (mm^{-1}) the respective PSD intercept and slope parameters (e.g., Heymsfield et al. 2008; Woods et al. 2008; Pettersen et al. 2020a). Higher N_o values indicate a larger population of smaller diameter particles, while lower Λ values define broader PSDs with larger diameter particles.

Adopting this PSD descriptor framework, Pettersen et al. (2020a) showed that deep KMQT snowfall events possess narrow PSDs with elevated smaller particle concentrations. Unlike deep events, shallow snow N_o–Λ relationships are distinctly bimodal. A primary cluster exhibits broad PSDs and low small particle concentrations, while a secondary cluster displays narrow PSDs and preferentially smaller particle diameters. This secondary shallow grouping is associated with extremely cold LES events that likely suppress dendritic particles due to a limited or nonexistent dendritic growth zone (i.e., ambient temperatures between about −12° and −18°C with sufficient supersaturation levels to support dendritic snowflake growth; Bailey and Hallett 2009) within shallow LES cloud structures. Rimed particle splintering or wind-induced particle fracturing may also inflate the smaller particle population.

Figures 10 reveals further regime-dependent microphysical variability measured by the PIP. SLR values are mostly near ~10 for deep KMQT snow events (Fig. 10a), while shallow events display more SLR variability as a function of PSD properties (Fig. 10b). Considerable variability
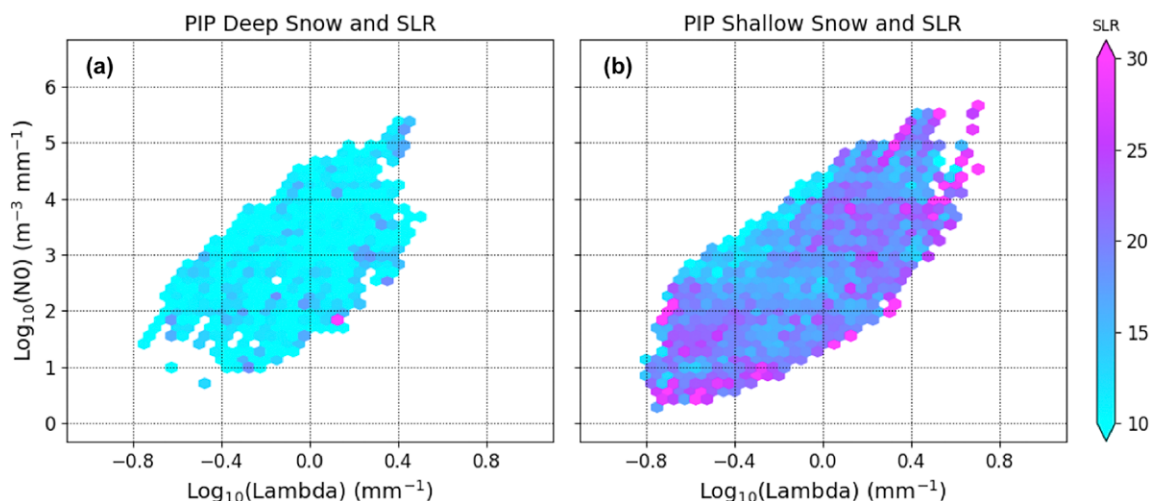

Fig. 10. Mean SLR as a function of PIP-derived PSD intercept parameter N_0 and slope parameter Λ for KMQT (a) deep and (b) shallow snowfall events during the January 2014–April 2018 period.
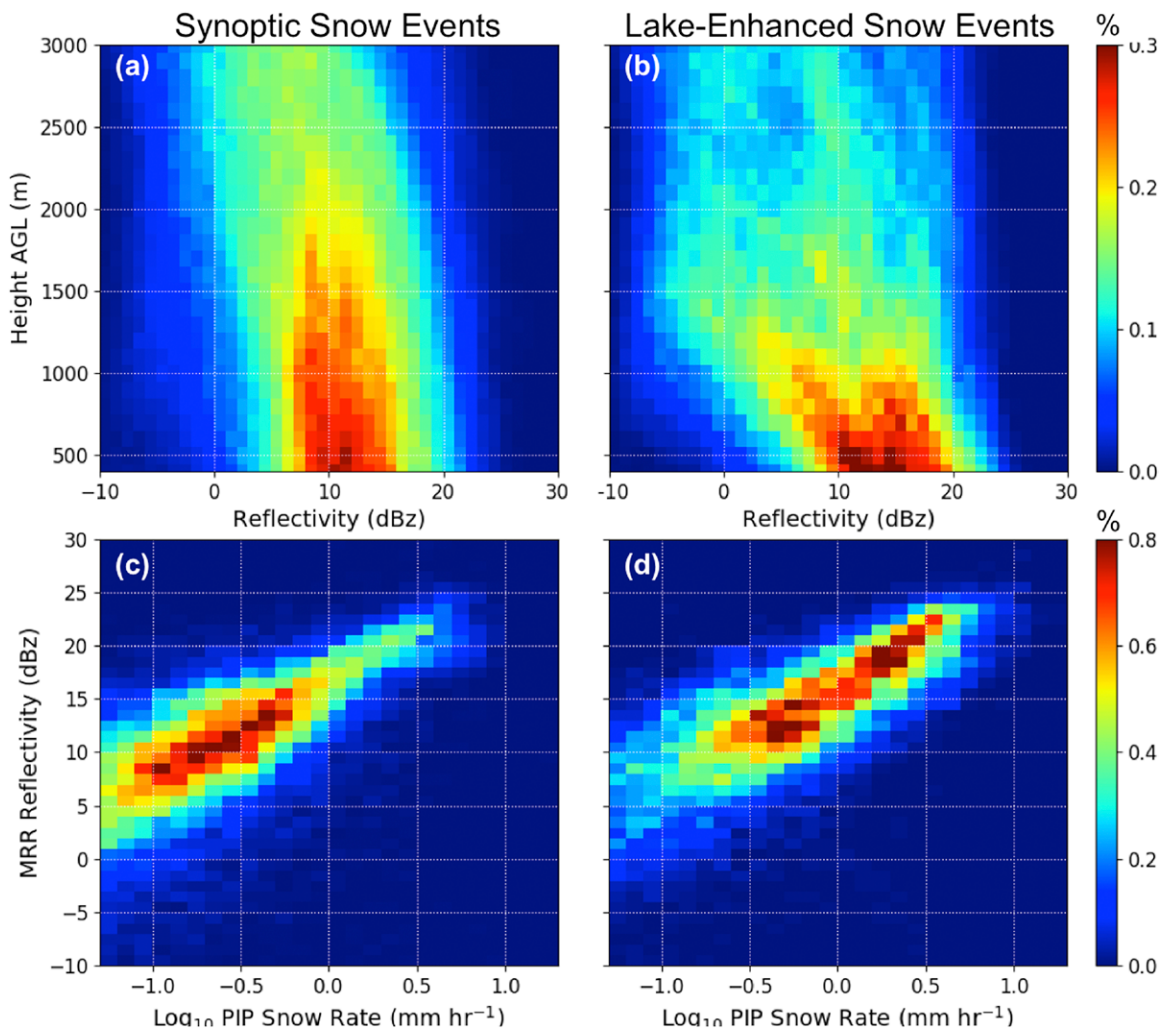
Fig. 11. As in Fig. 6, but for synoptic and lake-enhanced synoptic snowfall events.

exists across the entire shallow snow population, although the largest population of shallow events indicated by the Pettersen et al. (2020a) results have mean SLRs between ~20 and 25. These results offer a pathway to refine previous SLR climatologies based on daily manual measurements that indicate northern Great Lakes SLR values of ~17 (Baxter et al. 2005).

Lake-enhanced extreme snow events

Lake-enhanced snow is defined as synoptically generated snowfall that benefits from increased snowfall production via lake-orographic processes (Owens et al. 2017). Lake enhancement processes often amplify extreme KMQT snowfall events—typically midlatitude cyclones that track south and east of KMQT and produce prolonged NE winds—and appear as vertically aligned near-surface MRR reflectivity enhancements embedded within deeper synoptically forced fall streaks. KMQT MRR observations from 46 lake-enhanced and 150 nonenhanced synoptic events between January 2014 and April 2018 reveal Lake Superior's snowfall production role—likely combined with natural seeder–feeder processes—within synoptic snow events. MRR Z_{sfc} values are ~3–5 dB larger during lake-enhanced synoptic events compared to nonenhanced events (Figs. 11a,b). However, a secondary lake-enhanced mode exists with much larger Z_{sfc} values (~15–20 dBZ). Lake-enhanced events display ~6–8 dB km^{-1} MRR reflectivity enhancements in the lowest 1.5 km AGL, compared to ~2–3 dB km^{-1} for synoptic events. Similar to the orographic and LES snow categories, these large near-surface reflectivity gradients highlight spaceborne radar blind zone and range-dependent ground-based scanning radar QPE complications. MRR-PIP observations also accentuate the propensity for

lake-enhanced events to produce higher snowfall rates and slightly different Z–S relationships than nonenhanced synoptic events (Figs. 11c,d).

Figures 12 and 13 highlight an extreme lake-enhanced snowfall event on 10–12 November 2014 that produced 76 cm of accumulated snow at KMQT and warranted numerous winter
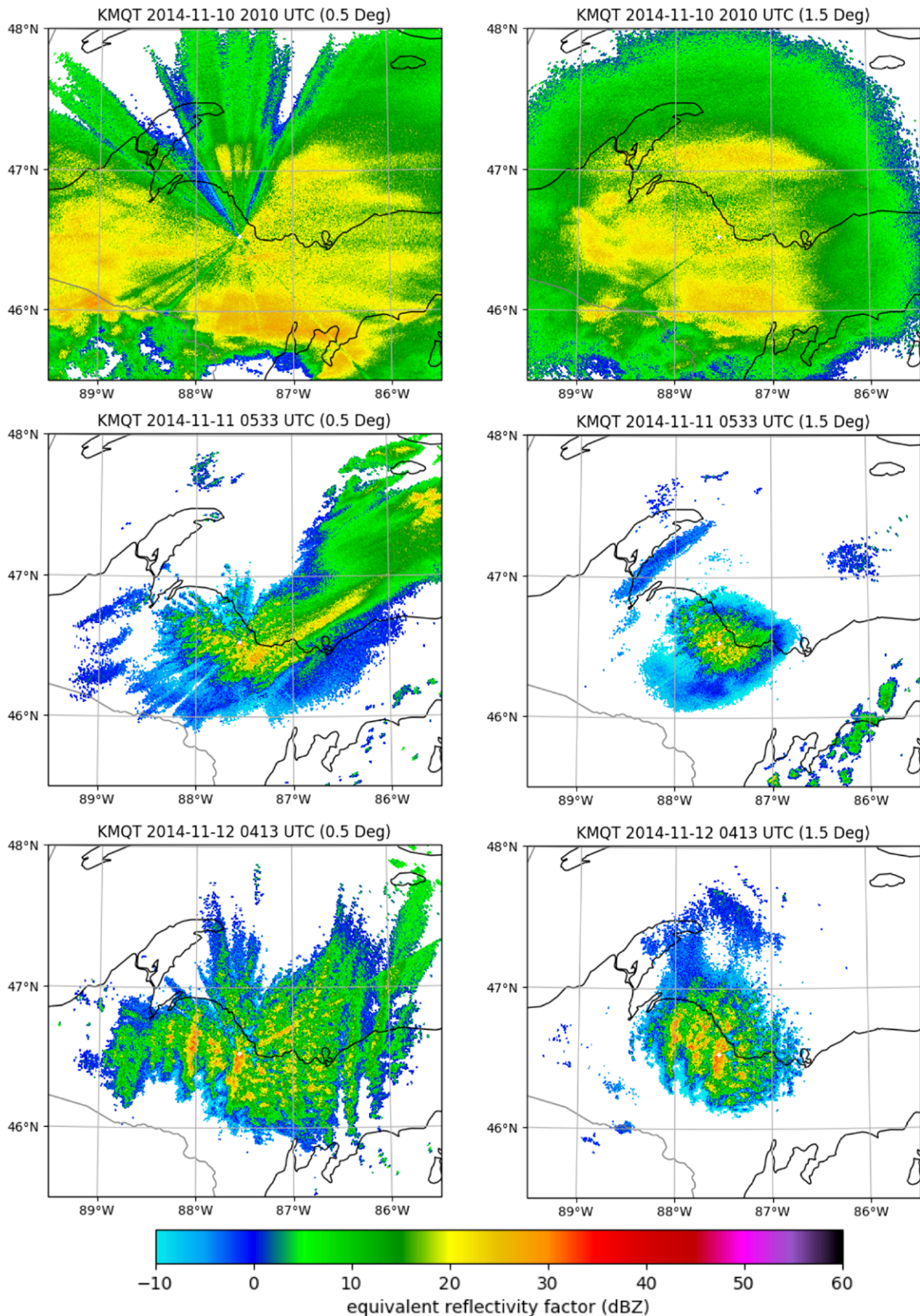

Fig. 12. KMQT (left) 0.5° and (right) 1.5° radar reflectivities for (top) 2000 UTC 10 Nov 2014, (middle) 0533 UTC 11 Nov 2014, and (bottom) 0413 UTC 12 Nov 2014.
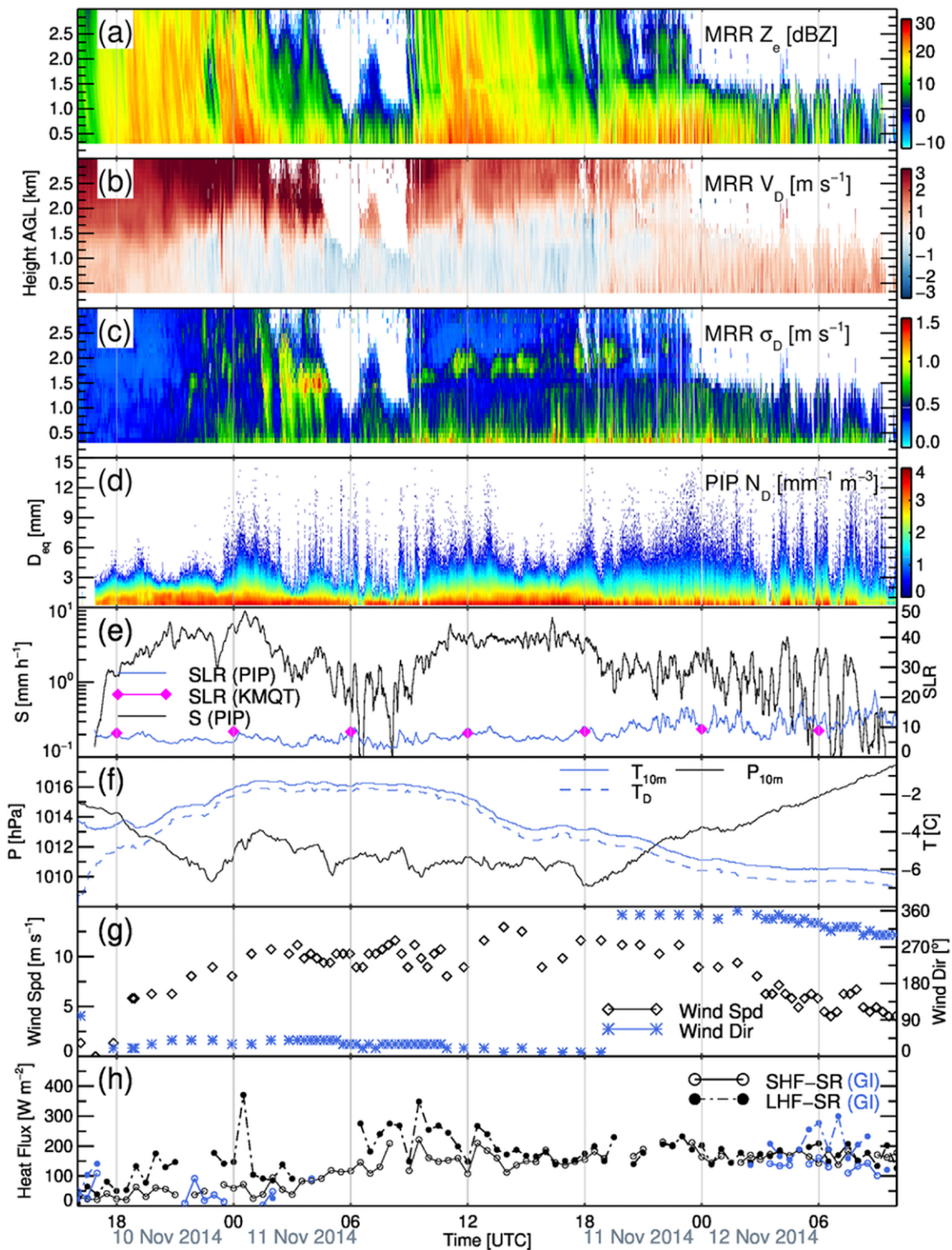
Fig. 13. As in Fig. 3, but for the 10–12 Nov 2014 lake-enhanced extreme snowfall event.

storm warnings and advisories. A complex and vigorous synoptic system skirted to the south, east, then northeast of KMQT (Fig. ES8) and followed a synoptic to LES event progression. The synoptic phase (1600–2300 UTC 10 November) produced widespread precipitation (Fig. 12 and Fig. ES9) and MRR-indicated fall streaks (Fig. 13a). PSDs were relatively narrow (Fig. 13d)—relatively few large particles were measured despite reflectivities in the 20–30 dBZ range and snowfall rates between ~2 and 8 mm h^{-1} (Fig. 13e). LES commenced after ~2300 UTC 11 November as temperatures continually decreased, surface pressure abruptly rose, winds shifted to the NNW–NW, and over-lake flux values exceeded ~200 W m^{-2} (Figs. 13f–h). The

PIP observed broad PSDs, larger particle diameters, and higher SLR values compared the synoptic period (Fig. 13e).

The most interesting period of this event, however, was the prolonged lake enhancement stage between ~2300 UTC 10 and 2300 UTC 11 November. This period was defined by increasingly intense NE winds (~10 m s^{-1}) during its early stages that produced 150–300 W m^{-2} over-lake fluxes (Figs. 13g,h). Lake enhancements appeared as shallow, periodic, and upright MRR reflectivity maxima embedded within deeper, slanted fall streaks (Fig. 13a). While this period is labeled as lake enhanced due to embedded MRR features that commenced after the NE wind shift and consequent air–lake interchanges, concurrent lake-orographic processes also likely increased snowfall production at KMQT. Mean reflectivities increased toward the ground by over 5 dB km^{-1} in the lowest 1.5 km AGL, compared to mostly invariant changes beforehand. MRR V_D and σ_D observations revealed a progressively agitated boundary layer throughout local nighttime hours (Figs. 13b,c). Localized σ_D maxima and MRR reflectivity minima were observed near ~1.5 km AGL, reflecting increased shear and turbulence at the boundary layer top. MRR observations were especially useful to delineate this period, as NEXRAD lake enhancement features were mostly obscured (Fig. ES9). NEXRAD observations, however, showed widespread synoptically forced snow before 0500 UTC 11 November and after 0900 UTC (Fig. 12 and Fig. ES9).

Notable PIP PSD changes also occurred as the storm evolved during and after the lake enhancement period (Figs. 13d,e). PSD's broadened near 2300 UTC 10 November as lake enhancements appeared in MRR profiles, with larger particle diameters and greater particle concentrations in the ~2–6-mm D_{eq} range. Extreme snowfall rates exceeded 10 mm h^{-1} early in the enhancement period, with sustained rates above ~5 mm h^{-1} between ~1000 and 1800 UTC 11 November. The PIP estimated SLR values between ~5 and 10, while KMQT measured SLR values near 10 throughout the entire storm. The lake-enhanced period contributed ~67% of the PIP-estimated snowfall accumulation during this event. The PIP (KMQT) measured 94.3 (82.3) mm LWE between 1800 UTC 10 and 1800 UTC 12 November.

Concluding remarks

This study introduces a ground-based instrumentation suite deployed in the northern Great Lakes region to investigate snowfall. Micro Rain Radar (MRR) and Precipitation Imaging Package (PIP) observations provide valuable profiling radar and snow microphysics observations in a previously understudied region that receives abundant snowfall from different regimes. The following scientific lessons learned are highlighted:

- *Snowfall from clouds with shallow vertical development is prevalent in the northern Great Lakes*. MRR profiles emphasize pervasive shallow snowfall (precipitation echo tops ~1.0–1.5 km) from mostly broad coverage lake-effect snow (LES) at KMQT. This snowfall is frequently light and can persist for long durations, but can also produce heavy snow and adverse conditions.
- *Lake-orographic processes influence snowfall production*. Lake-orographic processes instigate and enhance snowfall at KMQT. Unlike LES that exhibit discrete MRR reflectivity and banded NEXRAD features, lake-orographic snow at KMQT is typically shallow but more spatiotemporally contiguous. NEXRAD reflectivity enhancements are often anchored to shoreline topography. Coastal baroclinic processes also likely contribute to this snowfall mode.
- *Snow microphysical property variability is driven by regime-dependent processes*. Shallow snow events also contain preferentially larger particles than deep snow events, but also display notable microphysical and snow-to-liquid ratio (SLR) transformations under extremely cold conditions. PIP observations also reveal sudden snow microphysical changes

that are initiated by linked surface and atmospheric processes during lake enhancement events.

- *Lake enhancements accompany extreme snowfall events.* Lake enhancement processes are illustrated in multiple case studies and commonly occur during extreme snowfall events at this site. Lake enhancement signatures appear as near-surface reflectivity enhancements embedded within deeper synoptic snow features. Seeder–feeder particle growth mechanisms likely combine with lake-orographic influences to amplify surface snowfall rates compared to nonenhanced synoptic snow events.

- *Regime-dependent radar and microphysical variability complicates remote sensing QPE.* Regime-dependent Z–S differences underscore radar QPE ramifications. MRR reflectivities respond to microphysical changes, but some events exhibit similar near-surface reflectivity values despite markedly different microphysical composition. Shallow, light snow and near-surface enhancements embedded within deeper snow complicate spaceborne radar QPE. Near-surface reflectivity gradients of 7–10 dB km^{-1} within typical spaceborne radar blind zones are also observed in LES, lake-orographic, and lake enhanced events.

The strategically selected KMQT instrumentation package has capably produced a scientifically rich dataset. The MRR provides critical observations of near-surface snowfall processes, but are difficult to ascertain using NEXRAD or spaceborne observations. The PIP explicitly links remote sensing measurements with microphysical composition and provides independent snowfall rate and SLR estimates at high temporal resolution. GLEN observations add important air–lake energy exchange context to readily discern Lake Superior's influence on snowfall production. NEXRAD observations provide spatial context, while KMQT meteorological observations enable environmental factors to be investigated. KMQT snow accumulation measurements by trained meteorological staff provide crucial independent evaluation datasets. Collectively, the KMQT observatory enables snowfall regimes and transitions to be readily identified.

The KMQT dataset will be utilized extensively in future snowfall-related research. The dataset serves as a snow event occurrence and satellite quantitative precipitation estimation (QPE) evaluation site, especially to isolate regime-dependent biases (e.g., Henderson et al. 2017). Blind zone statistical studies applicable to current and future spaceborne radars will also be undertaken (e.g., Maahn et al. 2014). KMQT observations will also provide better microphysical constraints for QPE retrievals. Forward modeling chains that link frozen hydrometeor scattering models and observed particle size distributions to radar/radiometer observations will also be tested (e.g., Kulie et al. 2010; Olson et al. 2016). Refined Z–S relationships based on snowfall regime will improve NEXRAD QPE, while next-generation NEXRAD dual polarization snowfall rate estimators will also be evaluated.

Future projects will also focus on relatively unexplored topics. First, the KMQT dataset is well equipped to initiate multivariate analyses that quantify microphysical variability based on snowfall regime and environmental factors. Second, lake enhancement processes and their contribution to major snowstorms will be quantified by explicitly linking lake evaporation, boundary layer moistening and instability, natural cloud seeding, and coastal baroclinic effects. Third, numerical weather prediction parameterizations (microphysical, planetary boundary layer, land/surface schemes, etc.) that affect simulated lake-influenced snow production will be evaluated and improved using KMQT observational constraints (e.g., Reeves and Dawson 2013; Conrick et al. 2015; McMillen and Steenburgh 2015). KMQT observations will ultimately enable deeper knowledge of the linked processes that operate within northern Great Lakes snowfall regimes to improve predictive weather models and short-term forecasting.

References

Agee, E. M., and M. L. Hart, 1990: Boundary layer and mesoscale structure over Lake Michigan during a wintertime cold air outbreak. *J. Atmos. Sci.*, **47**, 2293–2316, https://doi.org/10.1175/1520-0469(1990)047<2293:BLAMSO>2.0.CO;2.

Angel, J. R., and S. A. Isard, 1998: The frequency and intensity of Great Lake cyclones. *J. Climate*, **11**, 61–71, https://doi.org/10.1175/1520-0442(1998)011<0061:TFAIOG>2.0.CO;2.

Bailey, M. P., and J. Hallett, 2009: A comprehensive habit diagram for atmospheric ice crystals: Confirmation from the laboratory, AIRS II, and other field studies. *J. Atmos. Sci.*, **66**, 2888–2899, https://doi.org/10.1175/2009JAS2883.1.

Ballentine, R. J., A. J. Stamm, E. E. Chermack, G. P. Byrd, and D. Schleede, 1998: Mesoscale model simulation of the 4–5 January 1995 lake-effect snowstorm. *Wea. Forecasting*, **13**, 893–920, https://doi.org/10.1175/1520-0434(1998)013<0893:MMSOTJ>2.0.CO;2.

Bard, L., and D. A. R. Kristovich, 2012: Trend reversal in Lake Michigan contribution to snowfall. *J. Appl. Meteor. Climatol.*, **51**, 2038–2046, https://doi.org/10.1175/JAMC-D-12-064.1.

Barthold, F. E., and D. A. R. Kristovich, 2011: Observations of the crosslake cloud and snow evolution in a lake-effect snow event. *Mon. Wea. Rev.*, **139**, 2386–2398, https://doi.org/10.1175/MWR-D-10-05001.1.

Battaglia, A., E. Rustemeier, A. Tokay, U. Blahak, and C. Simmer, 2010: PARSIVEL snow observations: A critical assessment. *J. Atmos. Oceanic Technol.*, **27**, 333–344, https://doi.org/10.1175/2009JTECHA1332.1.

Baxter, M. A., C. E. Graves, and J. T. Moore, 2005: A climatology of snow-to-liquid ratio for the contiguous United States. *Wea. Forecasting*, **20**, 729–744, https://doi.org/10.1175/WAF856.1.

Blanken, P. D., C. Spence, N. Hedstrom, and J. D. Lenters, 2011: Evaporation from Lake Superior: 1. Physical controls and processes. *J. Great Lakes Res.*, **37**, 707–716, https://doi.org/10.1016/j.jglr.2011.08.009.

Braham, R. R., 1990: Snow particle size spectra in lake effect snows. *J. Appl. Meteor.*, **29**, 200–207, https://doi.org/10.1175/1520-0450(1990)029<0200:SPSSIL>2.0.CO;2.

——, and M. J. Dungey, 1984: Quantitative estimates of the effect of Lake Michigan on snowfall. *J. Climate Appl. Meteor.*, **23**, 940–949, https://doi.org/10.1175/1520-0450(1984)023<0940:QEOTEO>2.0.CO;2.

——, and ——, 1995: Lake-effect snowfall over Lake Michigan. *J. Appl. Meteor. Climatol.*, **34**, 1009–1019, https://doi.org/10.1175/1520-0450(1995)034<1009:LESOLM>2.0.CO;2.

Brandes, E. A., K. Ikeda, G. Zhang, M. Schönhuber, and R. M. Rasmussen, 2007: A statistical and physical description of hydrometeor distributions in Colorado snowstorms using a video disdrometer. *J. Appl. Meteor. Climatol.*, **46**, 634–650, https://doi.org/10.1175/JAM2489.1.

Burnett, A. W., M. E. Kirby, H. T. Mullins, and W. P. Patterson, 2003: Increasing Great Lake–effect snowfall during the twentieth century: A regional response to global warming? *J. Climate*, **16**, 3535–3542, https://doi.org/10.1175/1520-0442(2003)016<3535:IGLSDT>2.0.CO;2.

Campbell, L. S., and W. J. Steenburgh, 2017: The OWLeS IOP2b lake-effect snowstorm: Mechanisms contributing to the Tug Hill precipitation maximum. *Mon. Wea. Rev.*, **145**, 2461–2478, https://doi.org/10.1175/MWR-D-16 -0461.1.

Changnon, S. A., Jr., and D. M. A. Jones, 1972: Review of the influences of the Great Lakes on weather. *Water Resour. Res.*, **8**, 360–371, https://doi.org/10.1029/ WR008i002p00360.

Colle, B. A., D. Stark, and S. E. Yuter, 2014: Surface microphysical observations within east coast winter storms on Long Island, New York. *Mon. Wea. Rev.*, **142**, 3126–3146, https://doi.org/10.1175/MWR-D-14-00035.1.

Conrick, R., H. D. Reeves, and S. Zhong, 2015: The dependence of QPF on the choice of boundary- and surface-layer parameterization for a lake-effect snowstorm. *J. Appl. Meteor. Climatol.*, **54**, 1177–1190, https://doi.org/10.1175/JAMC-D-14-0291.1.

Cooper, S. J., N. B. Wood, and T. S. L'Ecuyer, 2017: A variational technique to estimate snowfall rate from coincident radar, snowflake, and fall-speed observations. *Atmos. Meas. Tech.*, **10**, 2557–2571, https://doi.org/10.5194/amt-10-2557-2017.

Eichenlaub, V. L., 1970: Lake effect snowfall to the lee of the Great Lakes: Its role in Michigan. *Bull. Amer. Meteor. Soc.*, **51**, 403–412, https://doi.org/10.1175/1520-0477(1970)051<0403:LESTTL>2.0.CO;2.

Field, P., A. Heymsfield, and A. Bansemer, 2007: Snow size distribution parameterization for midlatitude and tropical ice clouds. *J. Atmos. Sci.*, **64**, 4346–4365, https://doi.org/10.1175/2007JAS2344.1.

Gorodetskaya, I. V., N. P. M. Van Lipzig, M. R. Van den Broeke, A. Mangold, W. Boot, and C. H. Reijmer, 2013: Meteorological regimes and accumulation patterns at Utsteinen, Dronning Maud Land, East Antarctica: Analysis of two contrasting years. *J. Geophys. Res. Atmos.*, **118**, 1700–1715, https://doi.org/10.1002/ jgrd.50177.

Grecu, M., W. S. Olson, S. J. Munchak, S. Ringerud, L. Liao, Z. Haddad, B. L. Kelley, and S. F. McLaughlin, 2016: The GPM combined algorithm. *J. Atmos. Oceanic Technol.*, **33**, 2225–2245, https://doi.org/10.1175/JTECH-D-16-0019.1.

Hamada, A., and Y. N. Takayabu, 2016: Improvements in detection of light precipitation with the Global Precipitation Measurement Dual-Frequency Precipitation Radar (GPM DPR). *J. Atmos. Oceanic Technol.*, **33**, 653–667, https://doi.org/10.1175/JTECH-D-15-0097.1.

Helmus, J. J., and S. M. Collis, 2016: The Python ARM Radar Toolkit (Py-ART), a library for working with weather radar data in the Python programming language. *J. Open Res. Software*, **4**, e25, https://doi.org/10.5334/jors.119.

Henderson, D. S., C. D. Kummerow, D. A. Marks, and W. Berg, 2017: A regime-based evaluation of TRMM oceanic precipitation biases. *J. Atmos. Oceanic Technol.*, **34**, 2613–2635, https://doi.org/10.1175/JTECH-D-16-0244.1.

Henne, P. D., F. S. Hu, and D. T. Cleland, 2007: Lake-effect snow as the dominant control of mesic-forest distribution in Michigan, USA. *J. Ecol.*, **95**, 517–529, https://doi.org/10.1111/j.1365-2745.2007.01220.x.

Heymsfield, A. J., P. Field, and A. Bansemer, 2008: Exponential size distributions for snow. *J. Atmos. Sci.*, **65**, 4017–4031, https://doi.org/10.1175/2008JAS2583.1.

——, C. Schmitt, A. Bansemer, and C. H. Twohy, 2010: Improved representation of ice particle masses based on observations in natural clouds. *J. Atmos. Sci.*, **67**, 3303–3318, https://doi.org/10.1175/2010JAS3507.1.

Hiley, M. J., M. S. Kulie, and R. Bennartz, 2011: Uncertainty analysis for *CloudSat* snowfall retrievals. *J. Appl. Meteor. Climatol.*, **50**, 399–418, https://doi.org/10 .1175/2010JAMC2505.1.

Holroyd, E. W., 1971: Lake-effect cloud bands as seen from weather satellites. *J. Atmos. Sci.*, **28**, 1165–1170, https://doi.org/10.1175/1520-0469 (1971)028<1165:LECBAS>2.0.CO;2.

Hou, A. Y., and Coauthors, 2014: The Global Precipitation Measurement Mission. *Bull. Amer. Meteor. Soc.*, **95**, 701–722, https://doi.org/10.1175/BAMS-D-13-00164.1.

Houze, R. A., Jr., and Coauthors, 2017: The Olympic Mountains Experiment (OLYMPEX). *Bull. Amer. Meteor. Soc.*, **98**, 2167–2188, https://doi.org/10.1175/ BAMS-D-16-0182.1.

Huang, G.-J., V. Bringi, D. Moisseev, W. Petersen, L. Bliven, and D. Hudak, 2015: Use of 2D-video disdrometer to derive mean density-size and Z_e–SR relations: Four snow cases from the light precipitation validation environment. *Atmos. Res.*, **153**, 34–48, https://doi.org/10.1016/j.atmosres.2014.07.013.

Hudak, D., H. Barker, P. Rodriguez, and D. Donovan, 2006: The Canadian CloudSat validation project. *Fourth European Conf. on Radar in Hydrology and Meteorology*, Barcelona, Spain, ERAD, P11.6, www.crahi.upc.edu/ERAD2006/ proceedingsMask/00165.pdf.

Keighton, S., and Coauthors, 2009: A collaborative approach to study northwest flow snow in the southern Appalachians. *Bull. Amer. Meteor. Soc.*, **90**, 979–992, https://doi.org/10.1175/2009BAMS2591.1.

Kelly, R. D., 1982: A single Doppler radar study of horizontal-roll convection in a lake-effect snow storm. *J. Atmos. Sci.*, **39**, 1521–1531, https://doi.org/10.1175/1520-0469(1982)039<1521:ASDRSO>2.0.CO;2.

——, 1984: Horizontal roll and boundary-layer interrelationships observed over Lake Michigan. *J. Atmos. Sci.*, **41**, 1816–1826, https://doi.org/10.1175/1520-0469(1984)041<1816:HRABLI>2.0.CO;2.

——, 1986: Mesoscale frequencies and seasonal snowfalls for different types of Lake Michigan snow storms. *J. Climate Appl. Meteor.*, **25**, 308–312, https:// doi.org/10.1175/1520-0450(1986)025<0308:MFASSF>2.0.CO;2.

Klugmann, D., K. Heinsohn, and H. J. Kirtzel, 1996: A low cost 24 GHz FM-CW Doppler radar rain profiler. *Contrib. Atmos. Phys.*, **61**, 247–253.

Kneifel, S., M. S. Kulie, and R. Bennartz, 2011a: A triple-frequency approach to retrieve microphysical snowfall parameters. *J. Geophys. Res.*, **116**, D11203, https://doi.org/10.1029/2010JD015430.

——, M. Maahn, G. Peters, and C. Simmer, 2011b: Observation of snowfall with a low-power FM-CW K-band radar (Micro Rain Radar). *Meteor. Atmos. Phys.*, **113**, 75–87, https://doi.org/10.1007/s00703-011-0142-z.

——, A. von Lerber, J. Tiira, D. Moisseev, P. Kollias, and J. Leinonen, 2015: Observed relations between snowfall microphysics and triple-frequency radar measurements. *J. Geophys. Res. Atmos.*, **120**, 6034–6055, https://doi.org/10.1002/2015JD023156.

Kolka, R. K., C. P. Giardina, J. D. McClure, A. Mayer, and M. F. Jurgensen, 2010: Partitioning hydrologic contributions to an 'old-growth' riparian area in the Huron Mountains of Michigan, USA. *Ecohydrology*, **3**, 315–324, https://doi.org/10.1002/eco.112.

Kristovich, D. A. R., 1993: Mean circulations of boundary-layer rolls in lake-effect snow storms. *Bound.-Layer Meteor.*, **63**, 293–315, https://doi.org/10.1007/ BF00710463.

——, and R. A. Steve, 1995: A satellite study of cloud-band frequencies over the Great Lakes. *J. Appl. Meteor.*, **34**, 2083–2090, https://doi.org/10.1175/1520-0450(1995)034<2083:ASSOCB>2.0.CO;2.

——, and N. F. Laird, 1998: Observations of widespread lake-effect cloudiness: Influences of lake surface temperature and upwind conditions. *Wea. Forecasting*, **13**, 811–821, https://doi.org/10.1175/1520-0434(1998)013<0811:OOW LEC>2.0.CO;2.

——, and Coauthors, 2000: The Lake-Induced Convection Experiment and the snowband Dynamics Project. *Bull. Amer. Meteor. Soc.*, **81**, 519–542, https:// doi.org/10.1175/1520-0477(2000)081<0519:TLCEAT>2.3.CO;2.

——, N. F. Laird, and M. R. Hjelmfelt, 2003: Convective evolution across Lake Michigan during a WIDESPREAD Lake-effect snow event. *Mon. Wea. Rev.*, **131**, 643–655, https://doi.org/10.1175/1520-0493(2003)131<0643:CEALM D>2.0.CO;2.

——, and Coauthors, 2017: The Ontario Winter Lake-effect Systems field campaign: Scientific and educational adventures to further our knowledge and prediction of lake-effect storms. *Bull. Amer. Meteor. Soc.*, **98**, 315–332, https://doi.org/10.1175/BAMS-D-15-00034.1.

——, L. Bard, L. Stoecker, and B. Geerts, 2018: Influence of Lake Erie on a Lake Ontario lake-effect snowstorm. *J. Appl. Meteor. Climatol.*, **57**, 2019–2033, https://doi.org/10.1175/JAMC-D-17-0349.1.

Kulie, M. S., and R. Bennartz, 2009: Utilizing spaceborne radars to retrieve dry snowfall. *J. Appl. Meteor. Climatol.*, **48**, 2564–2580, https://doi.org/10.1175 /2009JAMC2193.1.

——, and L. Milani, 2018: Seasonal variability of shallow cumuliform snowfall: A CloudSat perspective. *Quart. J. Roy. Meteor. Soc.*, **144**, 329–343, https://doi.org/10.1002/qj.3222.

——, R. Bennartz, T. Greenwald, Y. Chen, and F. Weng, 2010: Uncertainties in microwave optical properties of frozen precipitation: Implications for remote sensing and data assimilation. *J. Atmos. Sci.*, **67**, 3471–3487, https://doi.org/10.1175/2010JAS3520.1.

——, M. J. Hiley, R. Bennartz, S. Kneifel, and S. Tanelli, 2014: Triple-frequency radar reflectivity signatures of snow: Observations and comparisons with theoretical ice particle scattering models. *J. Appl. Meteor. Climatol.*, **53**, 1080–1098, https://doi.org/10.1175/JAMC-D-13-066.1.

——, L. Milani, N. B. Wood, S. A. Tushaus, R. Bennartz, and T. S. L'Ecuyer, 2016: A shallow cumuliform snowfall census using spaceborne radar. *J. Hydrometeor.*, **17**, 1261–1279, https://doi.org/10.1175/JHM-D-15-0123.1.

Kummerow, C. D., D. L. Randel, M. Kulie, N. Wang, R. Ferraro, S. Joseph Munchak, and V. Petkovic, 2015: The evolution of the Goddard profiling algorithm to a fully parametric scheme. *J. Atmos. Oceanic Technol.*, **32**, 2265–2280, https://doi.org/10.1175/JTECH-D-15-0039.1.

Kunkel, K. E., L. Ensor, M. Palecki, D. Easterling, D. Robinson, K. G. Hubbard, and K. Redmond, 2009: A new look at lake-effect snowfall trends in the Laurentian Great Lakes using a temporally homogeneous data set. *J. Great Lakes Res.*, **35**, 23–29, https://doi.org/10.1016/j.jglr.2008.11.003.

Laird, N. F., N. Metz, L. Gaudet, C. Grasmick, L. Higgins, C. Loeser, and D. Zelinsky, 2017: Climatology of cold season lake-effect cloud bands for the North American Great Lakes. *Int. J. Climatol.*, **37**, 2111–2121, https://doi.org/10.1002/joc.4838.

Lang, C. E., J. M. McDonald, L. Gaudet, D. Doeblin, E. A. Jones, and N. F. Laird, 2018: The influence of a lake-to-lake connection from Lake Huron on the lake-effect snowfall in the vicinity of Lake Ontario. *J. Appl. Meteor. Climatol.*, **57**, 1423–1439, https://doi.org/10.1175/JAMC-D-17-0225.1.

Leathers, D. J., and A. W. Ellis, 1996: Synoptic mechanisms associated with snowfall increases to the lee of Lakes Erie and Ontario. *Int. J. Climatol.*, **16**, 1117–1135, https://doi.org/10.1002/(SICI)1097-0088(199610)16:10<1117::AID-JOC80>3.0.CO;2-4.

Leinonen, J., S. Kneifel, D. Moisseev, J. Tyynela, S. Tanelli, and T. Nousiainen, 2012: Evidence of nonspheroidal behavior in millimeter-wavelength radar observations of snowfall. *J. Geophys. Res.*, **117**, D18205, https://doi.org/10.1029/2012JD017680.

Liao, L., R. Meneghini, A. Tokay, and L. F. Bliven, 2016: Retrieval of snow properties for Ku- and Ka-band dual-frequency radar. *J. Appl. Meteor. Climatol.*, **55**, 1845–1858, https://doi.org/10.1175/JAMC-D-15-0355.1.

Liu, G., 2008a: A database of microwave single-scattering properties for nonspherical ice particles. *Bull. Amer. Meteor. Soc.*, **89**, 1563–1570, https://doi.org/10.1175/2008BAMS2486.1.

——, 2008b: Deriving snow cloud characteristics from CloudSat observations. *J. Geophys. Res.*, **113**, D00A09, https://doi.org/10.1029/2007JD009766.

Maahn, M., and P. Kollias, 2012: Improved Micro Rain Radar snow measurements using Doppler spectra post-processing. *Atmos. Meas. Tech.*, **5**, 2661–2673, https://doi.org/10.5194/amt-5-2661-2012.

——, C. Burgard, S. Crewell, I. V. Gorodetskaya, S. Kneifel, S. Lhermitte, K. Van Tricht, and N. P. van Lipzig, 2014: How does the spaceborne radar blind zone affect derived surface snowfall statistics in polar regions? *J. Geophys. Res. Atmos.*, **119**, 13 604–13 620, https://doi.org/10.1002/2014JD022079.

Matrosov, S. Y., 2007: Modeling backscatter properties of snowfall at millimeter wavelengths. *J. Atmos. Sci.*, **64**, 1727–1736, https://doi.org/10.1175/JAS3904.1.

——, C. Campbell, D. Kingsmill, and E. Sukovich, 2009: Assessing snowfall rates from X-band radar reflectivity measurements. *J. Atmos. Oceanic Technol.*, **26**, 2324–2339, https://doi.org/10.1175/2009JTECHA1238.1.

——, M. Maahn, and G. de Boer, 2019: Observational and modeling study of ice hydrometeor radar dual-wavelength ratios. *J. Appl. Meteor. Climatol.*, **58**, 2005–2017, https://doi.org/10.1175/JAMC-D-19-0018.1.

McFarquhar, G. M., and Coauthors, 2017: Processing of ice cloud in situ data collected by bulk water, scattering, and imaging probes: Fundamentals, uncertainties, and efforts toward consistency. *Ice Formation and Evolution in Clouds and Precipitation: Measurement and Modeling Challenges*, Meteor. Monogr., No. 58, Amer. Meteor. Soc., https://doi.org/10.1175/AMSMONOGRAPHS-D-16-0007.1.

McMillen, J. D., and W. J. Steenburgh, 2015: Impact of microphysics parameterizations on simulations of the 27 October 2010 Great Salt Lake–effect snowstorm. *Wea. Forecasting*, **30**, 136–152, https://doi.org/10.1175/WAF-D-14-00060.1.

Meng, H., J. Dong, R. Ferraro, B. Yan, L. Zhao, C. Kongoli, N.-Y. Wang, and B. Zavodsky, 2017: A 1DVAR-based snowfall rate retrieval algorithm for passive microwave radiometers. *J. Geophys. Res. Atmos.*, **122**, 6520–6540, https://doi.org/10.1002/2016JD026325.

Minder, J. R., T. W. Letcher, L. S. Campbell, P. G. Veals, and W. J. Steenburgh, 2015: The evolution of lake-effect convection during landfall and orographic uplift as observed by profiling radars. *Mon. Wea. Rev.*, **143**, 4422–4442, https://doi.org/10.1175/MWR-D-15-0117.1.

Newman, A. J., P. A. Kucera, and L. F. Bliven, 2009: Presenting the Snowflake Video Imager (SVI). *J. Atmos. Oceanic Technol.*, **26**, 167–179, https://doi.org/10.1175/2008JTECHA1148.1.

Niziol, T. A., W. R. Snyder, and J. S. Waldstreicher, 1995: Winter weather forecasting throughout the eastern United States. Part IV: Lake effect snow. *Wea. Forecasting*, **10**, 61–77, https://doi.org/10.1175/1520-0434(1995)010<0061:WWFTTE>2.0.CO;2.

Norton, D. C., and S. J. Bolsenga, 1993: Spatiotemporal trends in lake effect and continental snowfall in the Laurentian Great Lakes, 1951–1980. *J. Climate*, **6**, 1943–1956, https://doi.org/10.1175/1520-0442(1993)006<1943:STILEA>2.0.CO;2.

Notaro, M., K. Holman, A. Zarrin, E. Fluck, S. Vavrus, and V. Bennington, 2013: Influence of the Laurentian Great Lakes on regional climate. *J. Climate*, **26**, 789–804, https://doi.org/10.1175/JCLI-D-12-00140.1.

——, D. Lorenz, C. Hoving, and M. Schummer, 2014: Twenty-first-century projections of snowfall and winter severity across central-eastern North America. *J. Climate*, **27**, 6526–6550, https://doi.org/10.1175/JCLI-D-13-00520.1.

Olson, W. S., and Coauthors, 2016: The microwave radiative properties of falling snow derived from nonspherical ice particle models. Part II: Initial testing using radar, radiometer and in situ observations. *J. Appl. Meteor. Climatol.*, **55**, 709–722, https://doi.org/10.1175/JAMC-D-15-0131.1.

Owens, N. D., R. M. Rauber, B. F. Jewett, and G. M. McFarquhar, 2017: The contribution of lake enhancement to extreme snowfall within the Chicago–Milwaukee urban corridor during the 2011 Groundhog Day blizzard. *Mon. Wea. Rev.*, **145**, 2405–2420, https://doi.org/10.1175/MWR-D-17-0025.1.

Pettersen, C., R. Bennartz, A. J. Merrelli, M. D. Shupe, D. D. Turner, and V. P. Walden, 2018: Precipitation regimes over central Greenland inferred from 5 years of ICECAPS observations. *Atmos. Chem. Phys.*, **18**, 4715–4735, https://doi.org/10.5194/acp-18-4715-2018.

——, M. S. Kulie, L. F. Bliven, A. J. Merrelli, W. A. Petersen, T. J. Wagner, D. B. Wolff, and N. B. Wood, 2020a: A composite analysis of snowfall modes from four winter seasons in Marquette, Michigan. *J. Appl. Meteor. Climatol.*, **59**, 103–124, https://doi.org/10.1175/JAMC-D-19-0099.1.

——, and Coauthors, 2020b: Introducing the Precipitation Imaging Package: Assessment of microphysical and bulk characteristics of snow. *Atmosphere*, **11**, 785, https://doi.org/10.3390/atmos11080785.

Petterssen, S., and P. A. Calabrese, 1959: On some weather influences due to warming of the air by the Great Lakes in winter. *J. Meteor.*, **16**, 646–652, https://doi.org/10.1175/1520-0469(1959)016<0646:OSWIDT>2.0.CO;2.

Reeves, H. D., and D. T. Dawson, 2013: The dependence of QPF on the choice of microphysical parameterization for lake-effect snowstorms. *J. Appl. Meteor. Climatol.*, **52**, 363–377, https://doi.org/10.1175/JAMC-D-12-019.1.

Ringerud, S., M. S. Kulie, D. L. Randel, G. S. Skofronick-Jackson, and C. D. Kummerow, 2019: Effects of ice particle representation on passive microwave precipitation retrieval in a Bayesian scheme. *IEEE Trans. Geosci. Remote Sens.*, **57**, 3619–3632, https://doi.org/10.1109/TGRS.2018.2886063.

Rodriguez, Y., D. A. R. Kristovich, and M. R. Hjelmfelt, 2007: Lake-to-lake cloud bands: Frequencies and locations. *Mon. Wea. Rev.*, **135**, 4202–4213, https://doi.org/10.1175/2007MWR1960.1.

Ryzhkov, A. V., and D. S. Zrnić, 2019: Polarimetric measurements of precipitation. *Radar Polarimetry for Weather Observations*, Springer Atmospheric Sciences, 373–433.

Schirle, C. E., S. J. Cooper, M. A. Wolff, C. Pettersen, N. B. Wood, T. S. L'Ecuyer, T. Ilmo, and K. Nygård, 2019: Estimation of snowfall properties at a mountainous site in Norway using combined radar and in situ microphysical observations. *J. Appl. Meteor. Climatol.*, **58**, 1337–1352, https://doi.org/10.1175/JAMC-D-18-0281.1.

Schmidlin, T. W., 1993: Impacts on severe winter weather during December 1989 in the Lake Erie snowbelt. *J. Climate*, **6**, 759–767, https://doi.org/10.1175/1520-0442(1993)006<0759:IOSWWD>2.0.CO;2.

——, and J. Kosarik, 1999: A record Ohio snowfall during 9–14 November 1996. *Bull. Amer. Meteor. Soc.*, **80**, 1107–1116, https://doi.org/10.1175/1520-0477(1999)080<1107:AROSDN>2.0.CO;2.

Schroeder, J. J., D. A. Kristovich, and M. R. Hjelmfelt, 2006: Boundary layer and microphysical influences of natural cloud seeding on a lake-effect snowstorm. *Mon. Wea. Rev.*, **134**, 1842–1858, https://doi.org/10.1175/MWR3151.1.

Scott, R. W., and F. A. Huff, 1996: Impacts on the Great Lakes on regional climate conditions. *J. Great Lakes Res.*, **22**, 845–863, https://doi.org/10.1016/S0380-1330(96)71006-7.

Skofronick-Jackson, G., and Coauthors, 2015: Global Precipitation Measurement Cold Season Precipitation Experiment (GCPEX): For measurement's sake, let it snow. *Bull. Amer. Meteor. Soc.*, **96**, 1719–1741, https://doi.org/10.1175/BAMS-D-13-00262.1.

——, and Coauthors, 2017: The Global Precipitation Measurement (GPM) mission for science and society. *Bull. Amer. Meteor. Soc.*, **98**, 1679–1695, https://doi.org/10.1175/BAMS-D-15-00306.1.

——, M. Kulie, L. Milani, S. J. Munchak, N. B. Wood, and V. Levizzani, 2019: Satellite estimation of falling snow: A Global Precipitation Measurement (GPM) *Core Observatory* perspective. *J. Appl. Meteor. Climatol.*, **58**, 1429–1448, https://doi.org/10.1175/JAMC-D-18-0124.1.

Sousounis, P. J., and J. M. Fritsch, 1994: Lake-aggregate mesoscale disturbances. Part II: A case study of the effects on regional and synoptic-scale weather systems. *Bull. Amer. Meteor. Soc.*, **75**, 1793–1812, https://doi.org/10.1175/1520-0477(1994)075<1793:LAMDPI>2.0.CO;2.

Souverijns, N., A. Gossart, S. Lhermitte, I. V. Gorodetskaya, S. Kneifel, M. Maahn, F. L. Bliven, and N. P. M. van Lipzig, 2017: Estimating radar reflectivity—Snowfall rate relationships and their uncertainties over Antarctica by combining disdrometer and radar observations. *Atmos. Res.*, **196**, 211–223, https://doi.org/10.1016/j.atmosres.2017.06.001.

Spence, C., P. D. Blanken, N. Hedstrom, V. Fortin, and H. Wilson, 2011: Evaporation from Lake Superior: 2: Spatial distribution and variability. *J. Great Lakes Res.*, **37**, 717–724, https://doi.org/10.1016/j.jglr.2011.08.013.

——, ——, J. D. Lenters, and N. Hedstrom, 2013: The importance of spring and autumn atmospheric conditions for the evaporation regime of Lake Superior. *J. Hydrometeor.*, **14**, 1647–1658, https://doi.org/10.1175/JHM-D-12-0170.1.

Stark, D., B. A. Colle, and S. E. Yuter, 2013: Observed microphysical evolution for two east coast winter storms and the associated snow bands. *Mon. Wea. Rev.*, **141**, 2037–2057, https://doi.org/10.1175/MWR-D-12-00276.1.

Stephens, G. L., and Coauthors, 2008: CloudSat mission: Performance and early science after the first year of operation. *J. Geophys. Res.*, **113**, D00A18, https://doi.org/10.1029/2008JD009982.

——, D. Winker, J. Pelon, C. Trepte, D. Vane, C. Yuhas, T. L'Ecuyer, and M. Lebsock, 2018: *CloudSat* and *CALIPSO* within the A-Train: Ten years of actively observing the Earth system. *Bull. Amer. Meteor. Soc.*, **99**, 569–581, https://doi.org/10.1175/BAMS-D-16-0324.1.

Suriano, Z. J., 2019: Changing intrasynoptic type characteristics and interannual frequencies of circulation patterns conducive to lake-effect snowfall. *J. Appl. Meteor. Climatol.*, **58**, 2313–2328, https://doi.org/10.1175/JAMC-D-19-0069.1.

——, and D. J. Leathers, 2017a: Synoptic climatology of lake effect snowfall conditions in the eastern Great Lakes region. *Int. J. Climatol.*, **37**, 4377–4389, https://doi.org/10.1002/joc.5093.

——, and ——, 2017b: Synoptically classified lake-effect snowfall trends to the lee of Lakes Erie and Ontario. *Climate Res.*, **74**, 1–13, https://doi.org/10.3354/cr01480.

Thomas, B. C., and J. E. Martin, 2007: A synoptic climatology and composite analysis of the Alberta clipper. *Wea. Forecasting*, **22**, 315–333, https://doi.org/10.1175/WAF982.1.

Tiira, J., D. N. Moisseev, A. von Lerber, D. Ori, A. Tokay, L. F. Bliven, and W. Petersen, 2016: Ensemble mean density and its connection to other microphysical properties of falling snow as observed in southern Finland. *Atmos. Meas. Tech.*, **9**, 4825–4841, https://doi.org/10.5194/amt-9-4825-2016.

Veals, P. G., and W. J. Steenburgh, 2015: Climatological characteristics and orographic enhancement of lake-effect precipitation east of Lake Ontario and over the Tug Hill Plateau. *Mon. Wea. Rev.*, **143**, 3591–3609, https://doi.org/10.1175/MWR-D-15-0009.1.

——, ——, and L. S. Campbell, 2018: Factors affecting the inland and orographic enhancement of lake-effect precipitation over the Tug Hill Plateau. *Mon. Wea. Rev.*, **146**, 1745–1762, https://doi.org/10.1175/MWR-D-17-0385.1.

Villani, J. P., M. L. Jurewicz Sr., and K. Reinhold, 2017: Forecasting the inland extent of lake effect snow bands downwind of Lake Ontario. *J. Oper. Meteor.*, **5**, 53–70, https://doi.org/10.15191/nwajom.2017.0505.

von Lerber, A., D. Moisseev, L. F. Bliven, W. Petersen, A. Harri, and V. Chandrasekar, 2017: Microphysical properties of snow and their link to Z_e–S relations during BAECC 2014. *J. Appl. Meteor. Climatol.*, **56**, 1561–1582, https://doi.org/10.1175/JAMC-D-16-0379.1.

——, ——, D. A. Marks, W. Petersen, A. M. Harri, and V. Chandrasekar, 2018: Validation of GMI snowfall observations by using a combination of weather radar and surface measurements. *J. Appl. Meteor. Climatol.*, **57**, 797–820, https://doi.org/10.1175/JAMC-D-17-0176.1.

Welsh, D., B. Geerts, X. Jing, P. T. Bergmaier, J. R. Minder, W. J. Steenburgh, and L. S. Campbell, 2016: Understanding heavy lake-effect snowfall: The vertical structure of radar reflectivity in a deep snowband over and downwind of Lake Ontario. *Mon. Wea. Rev.*, **144**, 4221–4244, https://doi.org/10.1175/MWR-D-16-0057.1.

West, T. K., W. J. Steenburgh, and G. G. Mace, 2019: Characteristics of sea-effect clouds and precipitation over the Sea of Japan region as observed by A-Train satellites. *J. Geophys. Res. Atmos.*, **124**, 1322–1335, https://doi.org/10.1029/2018JD029586.

Wolfe, J. P., and J. R. Snider, 2012: A relationship between reflectivity and snow rate for a high-altitude S-band radar. *J. Appl. Meteor. Climatol.*, **51**, 1111–1128, https://doi.org/10.1175/JAMC-D-11-0112.1.

Wood, N. B., and T. S. L'Ecuyer, 2021: What millimeter-wavelength radar reflectivity reveals about snowfall: An information-centric analysis. *Atmos. Meas. Tech.*, **14**, 869–888, https://doi.org/10.5194/amt-14-869-2021.

——, ——, F. L. Bliven, and G. L. Stephens, 2013: Characterization of video disdrometer uncertainties and impacts on estimates of snowfall rate and radar reflectivity. *Atmos. Meas. Tech.*, **6**, 3635–3648, https://doi.org/10.5194/amt-6-3635-2013.

——, ——, A. J. Heymsfield, and G. L. Stephens, 2015: Microphysical constraints on millimeter-wavelength scattering properties of snow particles. *J. Appl. Meteor. Climatol.*, **54**, 909–931, https://doi.org/10.1175/JAMC-D-14-0137.1.

Woods, C. P., M. T. Stoelinga, and J. D. Locatelli, 2008: Size spectra of snow particles measured in wintertime precipitation in the Pacific Northwest. *J. Atmos. Sci.*, **65**, 189–205, https://doi.org/10.1175/2007JAS2243.1.

Zhang, J., and Coauthors, 2016: Multi-Radar Multi-Sensor (MRMS) quantitative precipitation estimation: Initial operating capabilities. *Bull. Amer. Meteor. Soc.*, **97**, 621–638, https://doi.org/10.1175/BAMS-D-14-00174.1.